Geotechnical and Geological Engineering manuscript No.
(will be inserted by the editor)

A model of damage and healing coupling halite thermo-mechanical behavior to microstructure evolution

C. Zhu · C. Arson

Received: date / Accepted: date

Abstract Creep processes in halite (salt rock) include glide, cross-slip, diffusion and dynamic recrystallization. Diffusive Mass Transfer (DMT) can result in crack rebonding, and mechanical stiffness recovery. Crack rebonding driven by DMT occurs within a few days at room temperature and low pressure. DMT is enhanced at higher temperatures, which could be beneficial for the sustainabilty of geological storage facilities in salt mines. On the one hand, visco-plastic laws relating creep microscopic processes to microstructure changes are empirical. On the other hand, theoretical models of damage and healing disconnect thermodynamic variables from their physical meaning. The proposed model enriches the framework of Continuum Damage Mechanics (CDM) with fabric descriptors. In order to infer the form of fabric tensors from microstructure observation, creep tests were carried out on granular salt under constant stress and humidity conditions. The evolution of net damage is governed by a diffusion equation, in which the characteristic time scales with the typical size of halite crystals, and the diffusion coefficient is a function of temperature. A stress path comprising a tensile loading, a compressive unloading, a creep-healing stage and a reloading was simulated. Macroscopic and microscopic model predictions highlight the increased efficiency of healing with time and temperature. The model presented in this paper is expected to improve the fundamental understanding of damage and healing in rocks at both macroscopic and microscopic levels, and the long-term assessment of geological storage facilities.

C. Arson (corresonding author)
Georgia Institute of Technology
School of Civil & Environmental Engineering
790 Atlantic Drive
Atlanta, GA 30332-0355
Tel.: 404-385-0143
E-mail: chloe.arson@ce.gatech.edu

Keywords Continuum Damage Mechanics · temperature-assisted diffusion · healing · fabric tensor · microscopic observation · halite

1 Introduction

Wind is viewed as one of the green energies of the twenty-first century. A key sustainability issue raised in this type of technology is the mismatch between the periods of energy production and the periods of energy demand. Compressed Air Energy Storage (CAES) allows for the storage of the surplus of energy produced in periods of high wind for future use at peak hours. Salt rock caverns could ensure gas containment due to the favorable creep properties of halite (Cosenza et al. 1999; Bérest et al. 2001; Bérest et al. 2007, Succar and Williams 2008, Kim et al. 2012). Salt rock is also an attractive host rock for deep waste disposals, due to favorable creep characteristics and low gas permeability (Kwon and Wilson 1999; Hunsche and Hampel 1999; Chan et al. 2001; Yow and Hunt 2002; Hou 2003). However, the long-term behavior of salt rock cannot be elucidated with macroscopic laboratory tests, and requires an investigation of micro-level processes, completed by up-scaling methods. At the transition between primary and secondary creep, dislocation generation is balanced by cross-slip, diffusion and recrystallization processes. At low pressure, dislocation pile-ups and strain incompatibilities between grains induce stress concentrations resulting in dilatant micro-cracking. On the other hand, Diffusive Mass Transfer (DMT) not only can result in creep strain, but also can accelerate healing of cracks through local transfer of mass, and convert cracks into planar arrays of fluid inclusions. In salt rock, crack rebonding and consequent mechanical healing induced by DMT occur wihin a few days at room temperature and low pressure. DMT is enhanced at higher temperatures, which could be

beneficial for the sustainabilty of geological storage facilities in salt mines. Two groups of self-healing systems have been recognized so far (Voyiadjis et al. 2011), including active systems triggered by damage mechanisms (Kessler and White 2001), and passive systems requiring external stimulation. The damage and healing model proposed in this study belongs to the catagory of uncoupled passive system, analogous to the close-then-heal scheme proposed by Li and Uppu (2010).

The authors previously proposed a thermo-mechanical model to predict the effect of mechanical stress and temperature on crack opening and closure in rock (Zhu and Arson 2014), in which the effects of crack rebonding and microstructure evolution were not accounted for. In this study, the theoretical modeling framework is extended to couple halite thermo-mechanical behavior to microstructure evolution during crack debonding, opening, closure and rebonding. Section 2 provides an overview of the main strategies adopted in continuum mechanics to model microscopic processes observed in salt rock subject to creep. Section 3 explains the theoretical framework of the Continuum Damage Mechanics (CDM) model proposed herein to predict the effects of damage and healing on salt stiffness and deformation, at the scale of a Representative Elementary Volume (REV). Section 4 presents a statistical image analysis of salt microstructure, based on the observation of granular salt subject to creep. Microstructure descriptors identified in Section 4 are related to the thermodynamic variables employed in Section 3. The upscaling method is explained in detail in Section 5. A stress path comprising a tensile loading, a compressive unloading, a creep-healing stage and a reloading is simulated for different healing periods and temperatures. Results are discussed in Section 6.

2 Review of Damage and Healing Models in Salt Rock

2.1 Creep Processes (microscopic scale)

Four creep mechanisms were characterized experimentally in halite (Senseny et al. 1992, Fam et al., 1998), which occur over different ranges of temperature T and pressure σ (with μ as the shear modulus). These include (1) glide ($\sigma/\mu > 5 \cdot 10^{-4}; 273K < T < 853K$); (2) cross slip (high σ; $298K < T < 853K$); (3) diffusion ($\sigma/\mu < 5 \cdot 10^{-4}; T > 573K$); (4) dynamic recrystallization (low σ; high T). The proposed model focuses on dry salt at elevated temperature. In these conditions, DMT is expected to be the dominating mechanism for creep. Atoms and molecules migrate through the bulk of salt grains (volume diffusion, Nabarro-Herring creep) and along the grain boundaries (boundary diffusion, Coble creep). At the microscopic scale, DMT results in the rebonding of crack faces, and at the macroscopic scale, rebonding results in "healing", i.e. in the total or partial recovery of mechanical properties previously degraded by microcrack propagation.

Healing during DMT is usually described as the time-dependent counter effect of dilatant cracking, which can be modeled by visco-plastic deformation laws (Senseny et al. 1992, Hou 2003). During the healing process, wave velocities increase exponentially with time (Brodsky and Munson 1994) and elastic moduli also increase exponentially over time (Chan et al. 1998). Damaged elastic moduli can be related to wave velocities by means of O'Connell and Budiansky's (1974) homogenization scheme. However, homogenization does not explain the coupled evolution of microstructure and macroscopic variables. In the model proposed below, fabric descriptors are related to phenomenological variables, in order to distinguish the different phases of the mechanical recovery process, including crack closure and crack rebonding, with micro-cracks of different orientations and shapes.

2.2 Phenomenological Models (REV scale)

Laboratory tests have been conducted on halite under different temperatures for different durations to investigate the role of crack rebonding on strength (Fuenkajorn and Phueakphum, 2011), permeability (Chan et al. 2001; Schulze, 2007) and inelastic strains (Lux et al., 2000; Hou, 2003). Creep damage in salt has often been associated with inelastic dilatant deformation because deformation induced by dislocation creep is isochoric (Chan et al., 2001). Damage grows in stress states above the "dilatancy boundary", whereas below this boundary, the decrease of inelastic strains compensates damage deformation (Hou, 2003; Lux and Eberth, 2007). Damage cannot grow or decrease within the dilatancy boundary (Hunsche and Hampel, 1999). The model proposed by Chan et al. (1998) can predict the influence of creep and micro-crack propagation on deformation, but cannot account for the anisotropy induced by damage on strains and stiffness. A scalar damage variable is introduced in the model proposed by Hunsche and Hampel (1999) and Hou (2003), in order to describe material softening and define long-term creep failure. In the modeling approach of Miao et al. (1995), stiffness reduction is modeled within the framework of CDM, whereas inelastic deformation is considered to obey a plastic flow rule. Two dissipation potentials are necessary to close the formulation (one for CDM, one for plasticity).

In most constitutive models that account for creep, damage and healing, water content and brine saturation are not part of the thermodynamic variables. The dependence on temperature is based on experimental observations made in isothermal conditions. By contrast, a coupled thermo-mechanical thermodynamic framework was proposed by Zhou et al. (2011) to model creep and damage in geomaterials, and a thermo-mechanical model of crack opening and closure was pro-

posed by Zhu and Arson (2014). However, these models did not account for healing, defined herein as mechanical recovery resulting from crack rebonding.

3 Continuum Damage Model of Crack Debonding, Opening, Closure and Rebonding

3.1 Free energy and conjugation relationships

The model formulated in this paper couples microscopic and macroscopic thermo-mechanical evolution laws, in order to predict the effects of micro-crack debonding, opening, closure and rebonding on deformation and stiffness. The strain decomposition during a one dimensional stress path comprising a tensile strain followed by a compressive strain can be modeled as follows:

$$\varepsilon = \varepsilon^{\boldsymbol{el}} + \varepsilon^{\boldsymbol{d}} = \varepsilon^{\boldsymbol{el}} + \varepsilon^{\boldsymbol{ed}} + \varepsilon^{\boldsymbol{id}} \tag{1}$$

where the different strain terms are defined as shown in Figure 1. $\varepsilon^{\boldsymbol{el}}$ is the purely elastic strain, which would be fully recovered upon unloading with undamaged elastic moduli. Strain $\varepsilon^{\boldsymbol{d}}$ results from micro-crack propagation (i.e., damage) and has two components: $\varepsilon^{\boldsymbol{ed}}$ is the elastic strain induced by the degradation of elastic moduli with damage, and $\varepsilon^{\boldsymbol{id}}$ is the irreversible strain due to cracks that remain open even after the relaxation of tensile stress. The neutralization of irreversible damage-induced strain requires an additional compression stress, referred to as "residual stress" ($\boldsymbol{\sigma_R}$) in the following:

$$\boldsymbol{\sigma_R} = -\mathbb{C}(\boldsymbol{\Omega}) : \varepsilon^{id} \tag{2}$$

In which $\mathbb{C}$ is the elasticity tensor, noted $\mathbb{C}_0$ in the reference undamaged state, and $\mathbb{C}(\boldsymbol{\Omega})$ in the damaged state. The definition of the damage tensor $\boldsymbol{\Omega}$ will be explained in the following.

The free energy of the solid skeleton is the sum of the purely thermo-elastic deformation energy (ψ_s^{ET}) and the potential energy of crack faces ($\psi_s^{\Omega T}$). The latter depends on a second-order tensor of damage ($\boldsymbol{\Omega}$), and on a damage-induced deformation ($\varepsilon^{\boldsymbol{d}}$):

$$\begin{aligned}\psi_s &= \psi_s^{ET} + \psi_s^{\Omega T} \\ &= [\frac{1}{2}\varepsilon^{\boldsymbol{el}} : \mathbb{C}_0 : \varepsilon^{\boldsymbol{el}} - \frac{C_0\tau^2}{2\tau_0} - \tau \boldsymbol{K_0} : \varepsilon^{\boldsymbol{el}}] \\ &+ [\frac{1}{2}\varepsilon^{\boldsymbol{d}} : \mathbb{C}(\boldsymbol{\Omega}) : \varepsilon^{\boldsymbol{d}} - \frac{C(\boldsymbol{\Omega})\tau^2}{2\tau_0} - \tau \boldsymbol{K}(\boldsymbol{\Omega}) : \varepsilon^{\boldsymbol{d}}]\end{aligned} \tag{3}$$

In which τ is the temperature variation, and C is the heat capacity. The thermo-elastic properties of the damaged halite are expressed as:

$$C(\boldsymbol{\Omega}) = (1-n)C_s + nC_{air} \tag{4}$$

$$\boldsymbol{K}(\boldsymbol{\Omega}) = k(\boldsymbol{\Omega})\alpha_T \boldsymbol{\delta} \tag{5}$$

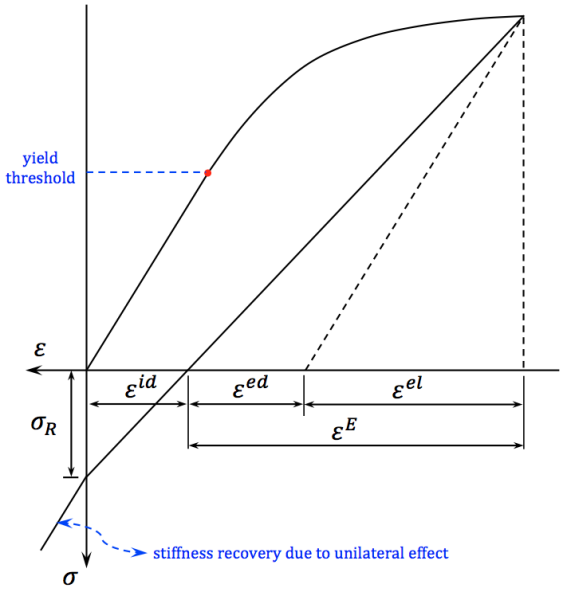

Fig. 1 Decomposition of deformation for a typical loading-unloading cycle. Note: the stress axis is pointing downwards, and the strain axis is pointing to the left; this corresponds to the the soil mechanics sign convention, in which compression is counted positive.

In which C_s is the heat capacity of the solid skeleton, C_{air} is the heat capacity of air, k is the bulk modulus, α_T is the thermal dilation coefficient, n is the porosity. $\boldsymbol{\delta}$ is the second-order identity tensor, and $\boldsymbol{K}$ is referred to as the "diagonal tensor" in the following. The deformation energy of the damaged halite is written:

$$\begin{aligned}\frac{1}{2}\varepsilon^{\boldsymbol{d}} : \mathbb{C}(\boldsymbol{\Omega}) : \varepsilon^{\boldsymbol{d}} &= \frac{1}{2}\lambda(tr\varepsilon^{\boldsymbol{d}})^2 + \mu\, tr(\varepsilon^{\boldsymbol{d}} \cdot \varepsilon^{\boldsymbol{d}}) \\ &+\alpha\, tr\varepsilon^{\boldsymbol{d}}\, tr(\varepsilon^{\boldsymbol{d}} \cdot \boldsymbol{\Omega}) + 2\beta\, tr(\varepsilon^{\boldsymbol{d}} \cdot \varepsilon^{\boldsymbol{d}} \cdot \boldsymbol{\Omega})\end{aligned} \tag{6}$$

In which λ and μ are Lamé coefficients (for the undamaged material), α and β are damage parameters. The stress and damage driving force tensors are obtained by thermodynamic conjugation (Collins and Houlsby, 1997):

$$\boldsymbol{\sigma} = \frac{\partial \psi_s}{\partial \varepsilon^{\boldsymbol{el}}} = \frac{\partial \psi_s^{ET}}{\partial \varepsilon^{\boldsymbol{el}}} = \mathbb{C}_0 : \varepsilon^{\boldsymbol{el}} - \tau \boldsymbol{K_0} \tag{7}$$

$$\begin{aligned}\boldsymbol{Y} &= -\frac{\partial \psi_s}{\partial \boldsymbol{\Omega}} = -\frac{\partial \psi_s^{\Omega T}}{\partial \boldsymbol{\Omega}} \\ &= -\left[\mathbb{C}(\boldsymbol{\Omega}) : \varepsilon^{\boldsymbol{d}}\right] : \frac{\partial \varepsilon^d}{\partial \boldsymbol{\Omega}} - \frac{1}{2}\varepsilon^{\boldsymbol{d}} : \frac{\partial \mathbb{C}(\boldsymbol{\Omega})}{\partial \boldsymbol{\Omega}} : \varepsilon^{\boldsymbol{d}} \\ &+ \frac{\tau^2}{2\tau_0}\frac{\partial C(\boldsymbol{\Omega})}{\partial \boldsymbol{\Omega}} + \tau \boldsymbol{K}(\boldsymbol{\Omega}) : \frac{\partial \varepsilon^{\boldsymbol{d}}}{\partial \boldsymbol{\Omega}} + \tau \frac{\partial \boldsymbol{K}(\boldsymbol{\Omega})}{\partial \boldsymbol{\Omega}} : \varepsilon^{\boldsymbol{d}}\end{aligned} \tag{8}$$

In the range of magnitudes of rock thermo-elastic moduli, the quadratic term in temperature $\frac{\tau^2}{2\tau_0}\frac{\partial C(\boldsymbol{\Omega})}{\partial \boldsymbol{\Omega}}$ is negligible in front of the other terms in the expression of the damage driving force. For simplicity, the damage criterion used in the following is based on a purely mechanical threshold. The damage force used is further simplified into:

$$\boldsymbol{Y_d} = -(\alpha + 2\beta)\varepsilon : \varepsilon \tag{9}$$

In which $\boldsymbol{Y_d}$ is called the "active" driving force in the following.

3.2 Damage propagation

The energy that needs to be released for micro-cracks to grow cumulates as damage propagates. In order to capture this hardening phenomenon, the propagation criterion is expressed as a linear function of damage:

$$f_d(\boldsymbol{Y_d}, \boldsymbol{\Omega}) = \sqrt{\frac{1}{2}\boldsymbol{Y_d} : \boldsymbol{Y_d}} - [a_0 + a_1 tr(\boldsymbol{\Omega})] \tag{10}$$

In which a_0 is the initial damage threshold, and a_1 is a parameter controlling the hardening rate. Following a classical CDM assumption (Dragon et al. 2000; Shao and Rudnicki 2000; Arson and Gatmiri 2009; Arson and Gatmiri 2012), the damage flow rule is assumed to be associative, i.e., f_d is used as a damage potential:

$$\begin{aligned} d\boldsymbol{\Omega} &= d\lambda_d \frac{\partial f_d(\mathbf{Y_d}, \boldsymbol{\Omega})}{\partial \mathbf{Y_d}} \\ &= \frac{\left[\frac{\mathbf{Y_d}}{\sqrt{2\mathbf{Y_d}:\mathbf{Y_d}}}\right] : d\mathbf{Y_d}}{a_1\boldsymbol{\delta} : \left[\frac{\mathbf{Y_d}}{\sqrt{2\mathbf{Y_d}:\mathbf{Y_d}}}\right]} : \left[\frac{\mathbf{Y_d}}{\sqrt{2\mathbf{Y_d} : \mathbf{Y_d}}}\right] \end{aligned} \tag{11}$$

The damage multiplier writes:

$$d\lambda_d = -\frac{\frac{\partial f_d}{\partial \mathbf{Y_d}} : d\mathbf{Y_d}}{\frac{\partial f_d}{\partial \boldsymbol{\Omega}} : \frac{\partial f_d}{\partial \mathbf{Y_d}}} = \frac{\mathbf{Y_d} : d\mathbf{Y_d}}{(a_1\boldsymbol{\delta}) : \mathbf{Y_d}} \tag{12}$$

Note that the active damage force can be given a more sophisticated expression to account for the decrease of fracture toughness observed in rock when temperature increases (Zhu and Arson 2013). Moreover, the implications of choosing an associate flow rule in anisotropic damage models is discussed in Xu and Arson (2014).

3.3 Unilateral effects of crack closure

In the model proposed herein, cracks are assumed to be closed when their faces are in contact but not bonded. Unilateral effects refer to the recovery of material compressive strength due to the closure of tensile cracks (Fig. 1). Following Chaboche's (1992) approach, the expression of stiffness shall depend on a Heaviside function to distinguish behaviors in tension and compression. Crack closure increases the number of intergranular contacts in the REV, which also results in a recovery of heat capacity:

$$\begin{aligned} \mathbb{C}^*(\boldsymbol{\Omega}) &= \mathbb{C}(\boldsymbol{\Omega}) \\ &\quad + \sum_{i=1}^{3} H(-tr(\boldsymbol{P_i} : \boldsymbol{\varepsilon}))\boldsymbol{P_i} : (\mathbb{C}_0 - \mathbb{C}(\boldsymbol{\Omega})) : \boldsymbol{P_i} \end{aligned} \tag{13}$$

$$\begin{aligned} C^*(\boldsymbol{\Omega}) &= C(\boldsymbol{\Omega}) \\ &\quad + \sum_{i=1}^{3} H(-tr(\boldsymbol{P_i} : \boldsymbol{\varepsilon}))\boldsymbol{P_i} : [(C_0 - C(\boldsymbol{\Omega}))\boldsymbol{\delta} \otimes \boldsymbol{\delta}] : \boldsymbol{P_i} \end{aligned} \tag{14}$$

(15)

In which $H(.)$ is the Heaviside function, $\boldsymbol{P_i}$ is the fourth order projection tensor for the projection in crack planes normal to direction i.

3.4 Mechanical recovery by crack rebonding

In the model proposed herein, damage is a rate-independent dissipation variable. The consistency equations impose that damage cannot decrease. Crack closure is the result of the normal displacement of open cracks faces under compression, which is assumed to produce an elastic deformation at the REV scale. Healing does not occur during crack closure, i.e. unilateral effects are not synonymous of mechanical recovery. Crack rebonding requires an energy input to trigger the migration of ions within the lattice, and is therefore a dissipative process independent from damage (Arson et al., 2012). As a result, the free energy of the REV shall depend on two state variables (purely elastic deformation $\boldsymbol{\varepsilon^{el}}$, temperature change τ) and two dissipation variables (damage $\boldsymbol{\Omega}$, healing $\mathbf{H}$). At low moisture content, crack rebonding in salt is mainly driven by DMT, as mentioned in the brief literature review above. DMT results from the migration of ions from the intact rock lattice to crack faces, either by volume diffusion or by boundary diffusion. Electronic attraction forces between different ionic species at crack faces tend to seal the cracks. At the scale of a typical rock sample ($\sim 10^{-2}$ m), intra-granular diffusion can be considered as an isotropic phenomenon because of the uniform distribution of grain orientations. Therefore, the healing tensor reduces to a scalar: $\boldsymbol{H} = h\,\boldsymbol{\delta}$. In order to describe mechanical stiffness recovery, a mixed damage variable $\boldsymbol{A}$ (also called "net damage" in CDM) is defined: $\boldsymbol{A}$ is the difference between damage (rate-independent) and healing h (rate-dependent, and activated only when cracks are closed):

$$\boldsymbol{A} = \boldsymbol{\Omega} - h\boldsymbol{\delta} \tag{16}$$

The final expressions of the damaged stiffness tensor and heat capacity depend on $\boldsymbol{A}$ instead of $\boldsymbol{\Omega}$:

$$\overline{\mathbb{C}}(\boldsymbol{A}) = \mathbb{C}(\boldsymbol{A}) + \sum_{i=1}^{3} H(-tr(\boldsymbol{P_i} : \varepsilon))\boldsymbol{P_i} : (\mathbb{C}_0 - \mathbb{C}(\boldsymbol{A})) : \boldsymbol{P_i} \quad (17)$$

$$\overline{C}(\boldsymbol{A}) = C(\boldsymbol{A}) + \sum_{i=1}^{3} H(-tr(\boldsymbol{P_i} : \varepsilon))\boldsymbol{P_i} : [(C_0 - C(\boldsymbol{A}))\boldsymbol{\delta} \otimes \boldsymbol{\delta}] : \boldsymbol{P_i} \quad (18)$$

The CDM healing variable h is related to healing-induced deformation, defined as a "counter-acting" damage deformation. A hypothetical stress-strain curve under the one-dimensional stress path shown in Figure 2 is plotted in Figure 3 to illustrate this concept. It should be noted that Figure 3 is purely conceptual and does not reflect exactly the trends of the model presented in the following (especially for the damage threshold during the reloading phase following the healing phase). Under tension, the specimen behaves elastically (OA) until damage starts to develop (AB). When tensile stress is released (BC), no additional damage is produced, but residual cracks remain open. The irreversible damage deformation (OC) can be compensated by applying an additional compression stress (CD). At state D, the deformation induced by residual crack openings is neutralized. Compression beyond that point (DE) results in unilateral effects: rigidity is recovered under compression. At E, the specimen is maintained between two fixed vertical plates, with no lateral confining stress. Creep processes at constant temperature occur over time, under constant axial deformation. Figure 3 shows a hypothetical stress path, in which creep processes do not significantly change the axial stress (EF), but result in mechanical healing (as can be seen from the reloading path in tension). As long as the axial stress is compressional (FG), the slope of the stress/strain remains the same as for the compressive stress path (DE). At the beginning of the tensile phase (GG_1), the slope angle of the stress strain curve lies between that of the undamaged material (OA) and that of the damaged material (AB), due to the partial mechanical recovery. When the recovered tension strength is reached, damage propagates again (G_1H).

For a given state of stress after a loading-unloading-creep-reloading cycle (σ_1 in Figure 3), the healing deformation ($\boldsymbol{\varepsilon^h}$) is defined as the difference between the deformation in the absence of healing, and the deformation observed after DMT has occurred:

$$\mathbb{C}(\boldsymbol{\Omega}) : \boldsymbol{\varepsilon^E} = \mathbb{C}(\boldsymbol{A}) : (\boldsymbol{\varepsilon^E} - \boldsymbol{\varepsilon^h}) \quad (19)$$

After substituting the expression of the net damage variable $\mathbf{A}$ and of the damaged stiffness tensor $\mathbb{C}(\boldsymbol{\Omega})$ into Eq. 19, the following relationship between the healing variable h and

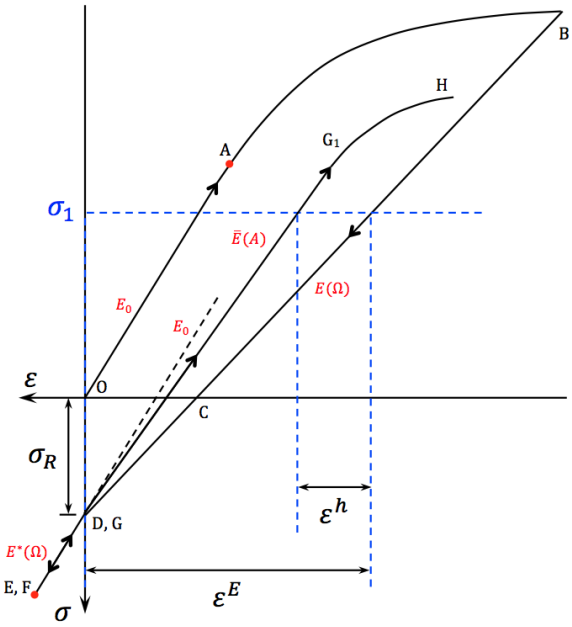

Fig. 3 Hypothetical stress/strain curve for the stress path illustrated in Fig. 2. E stands for the Young's modulus: E_0 - undamaged material; $E(\Omega)$ - damaged material; $E^*(\Omega)$ - damaged material with unilateral effect; $\overline{E}(A)$ - healed material. Note: the stress axis is pointing downwards, and the strain axis is pointing to the left; this corresponds to the the soil mechanics sign convention, in which compression is counted positive.

healing deformation ε_1^h is obtained:

$$h = \frac{3(\lambda + 2\mu)\varepsilon_1^h + (2\alpha + 4\beta)\varepsilon_1^h tr(\boldsymbol{\Omega})}{(2\alpha + 4\beta)(\varepsilon_v^E + 3\varepsilon_1^h)} \quad (20)$$

In which ε_v^E is the volumetric elastic deformation. Note that the proposed definition of healing deformation is not the classical definition of creep healing used in constitutive viscoplastic models of salt rock (e.g. Senseny et al. 1992; Hou 2003). The macroscopic and microscopic definitions of the deformation components are summarized in Table 1.

4 Evolution of Table Salt Microstructure during Creep

Deformation, damage and healing are sought in the form of functions of salt fabric descriptors. Fabric descriptors are sought in the form of moments of probability of geometric parameters of salt microstructure. Specific probability functions are obtained by analyzing microscope observations of halite crystals during creep tests carried out on table salt. These preliminary experiments are used to illustrate the concept of fabric-based damage and healing mechanics adopted in the model. Due to the relationship between thermodynamic variables and fabric descriptors, the model explains the evolution of salt microstructure during rate independent

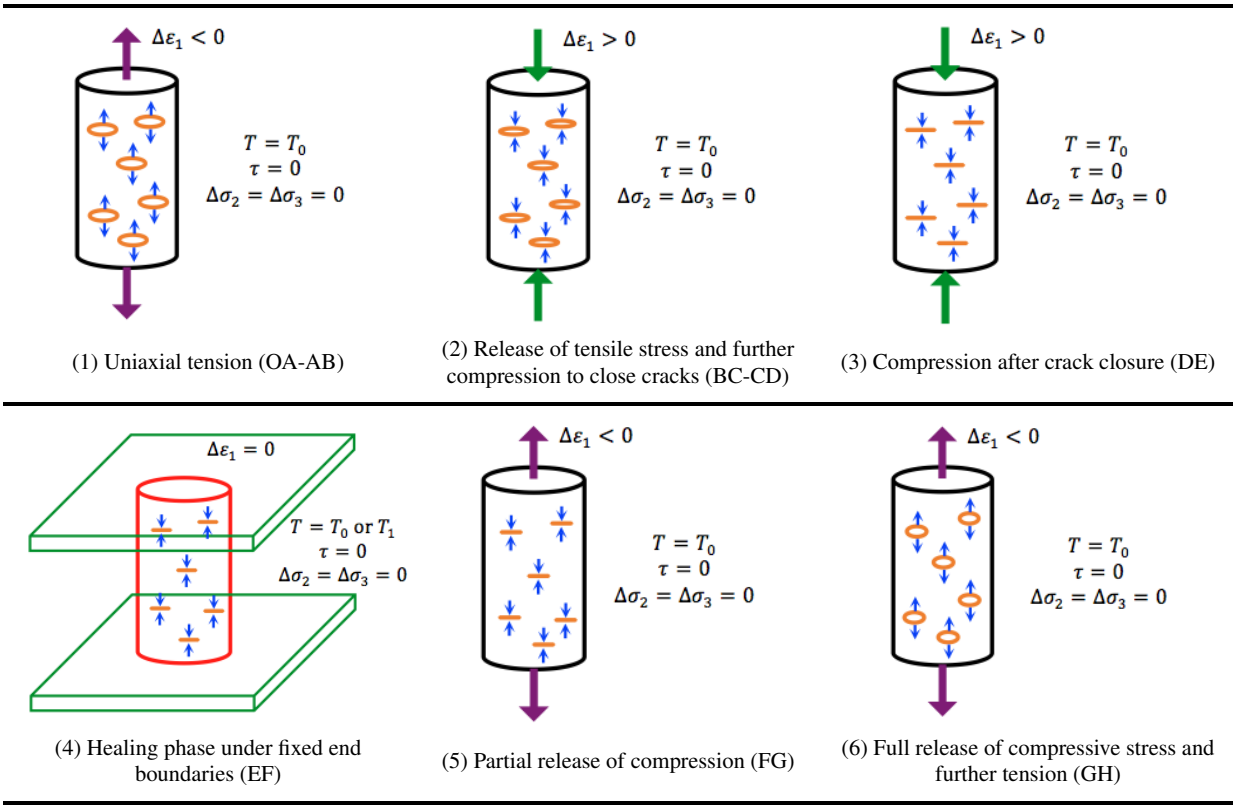

Fig. 2 Stress path simulated to study thermo-mechanical crack debonding, opening, closure, and healing

damage and creep healing (cf. Section 5). Consequent softening and mechanical recovery can be predicted (cf. Section 6). The high number of solid/solid interfaces contained in a sample of table salt ensures the statistical homogeneity of the REV: granular assemblies provide analogs of solids containing a large number micro-cracks. Future investigations will include tests on salt rock and crushed rock.

4.1 Experimental Set-Up

Table salt creep tests were carried out under constant stress. Salt particles were confined in tubes with both ends fixed by nails, as illustrated in Figure 4. The tubes were placed in a chamber with controlled moisture conditions at room temperature ($293K$). Constant humidity was ensured by placing saturated salt water at the bottom of the container, as explained by Wexler and Hasegawa (1954). The compressive load was applied at the top and bottom of the sample, by means of two rods: the bottom rod was fixed, and the top rod was connected to a spring of fixed length. All springs had the same rigidity. Three different initial elongations were chosen in order to apply three different pressures: 0.1MPa, 0.15MPa, 0.2MPa. The leave out between the rods and the tubes ensured constant exposure to moist, and was smaller than that the grain size, to avoid particle leakage.

The initial length of the sample was 19.1mm. After 120 days, the length was 16.8mm, 16.3mm, and 15.7mm for the samples subjected to 0.1MPa, 0.15MPa and 0.2MPa respectively. Therefore, it should be noted that, due to the deformation of the compressed spring, the experiments were not exactly creep tests. However the shortening of the sample in the early stages of the tests was considered as sufficiently small to attibute the rearrangement and rebonding of the grains to creep processes. At regular time intervals, the samples were observed with a stereomicroscope through the Plexiglas tube, on the lateral boundary of the specimens. For the three pressures tested, grains first rearranged to form a close packing, as shown in Figures 5a and 5b. After 120 days, bonds were observed between particles in contact (Figure 5c).

4.2 Image Processing

Due to their transparency and planar surfaces, table salt particles reflected the light transmitted during the stereoscopic observations. To improve the accuracy of the image analysis, photographs were processed with *ImageJ* application (Abramoff et al. 2004). An example is presented in Figure 6a. After enhancing the contrast and removing the background, the binary image shown in Figure 6b was obtained. A better quality image was achieved after removing outliers

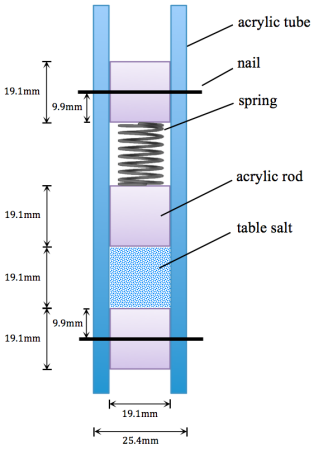

(a) Sketch of the spring system designed for the creep tests

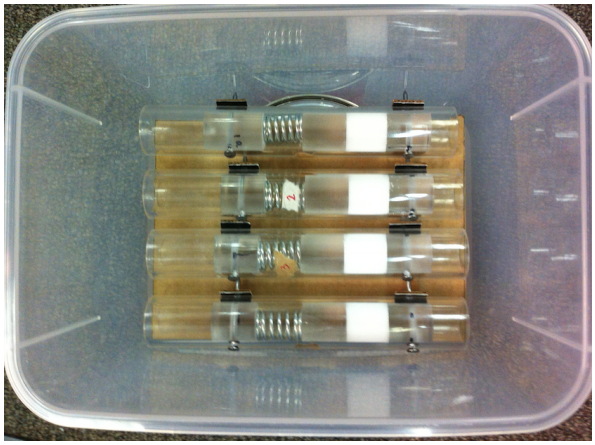

(b) Photo of the samples in the container (Lg. 215.9mm, Wd. 158.8mm, Ht. 228.6mm). Different elongations correspond to different loads. One trial sample was made for a pressure 0.2 MPa.

Fig. 4 Experimental set-up for the creep tests performed on table salt

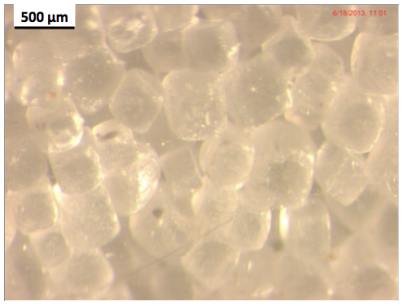

(a) June 18, 2013 (18 days)

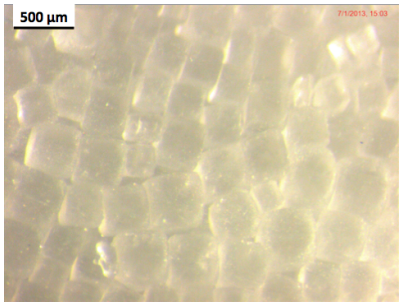

(b) July 1, 2013 (31 days)

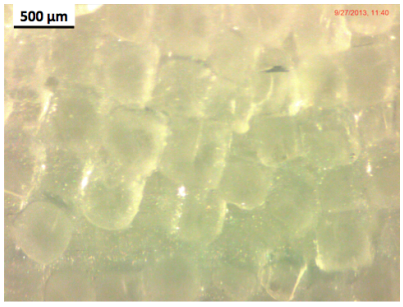

(c) September 27, 2013 (120 days)

Fig. 5 Qualitative microscopic observation of creep in table salt: (a) Early stages, loose packing; (b) Rearrangement towards a close packing; (c) Particle bonding (healing). *Note: Although the photos were not taken at the same location, similar phenomena were observed in all samples.*

and filling holes, as shown in Figure 6c: the black regions indicate the presence of void space between salt grains (which appear in white). Void outlines were plotted and numbered (Figure 6d), which allowed a quantitative geometrical analysis of salt microstructure during creep.

4.3 Image Analysis

After testing several shapes, it was found that the juxtaposition of fitting ellipses provided the best match with void contours. Statistical results indicate that the probability density function of ellipses' area ("void area", A_v) follows a power law distribution (Figure 7a):

$$p_A(A_v) = a \cdot A_v^t \tag{21}$$

For high values of A_v, the power law does not fit the experimental data as well as for smaller values of A_v. Since the probability density function was plotted in a log scale, the error was found acceptable. Fitting of microscopic data provided: $a = 5 \times 10^{-5}$ and $t = -1.2$. Despite the existence of several spikes, the projections of the major semi-axes in three principal directions of space (referred to as "crack length" in the following: R_i, $i = x, y, z$) were found to follow a lognormal distribution (Figure 7b):

$$p_i(R_i) = \frac{1}{\sqrt{2\pi} R_i s_i} e^{-\frac{(lnR_i - m_i)^2}{2s_i^2}} \tag{22}$$

In which s_i is the standard deviation and m_i is the mean value.

5 A Fabric-Based Model of Damage and Healing

5.1 Mechanisms driving fabric changes

Microscopic observations on granular salt are used as analogs to model mechanical recovery upon crack closure and re-bonding in salt rock: grain rearrangement represents crack

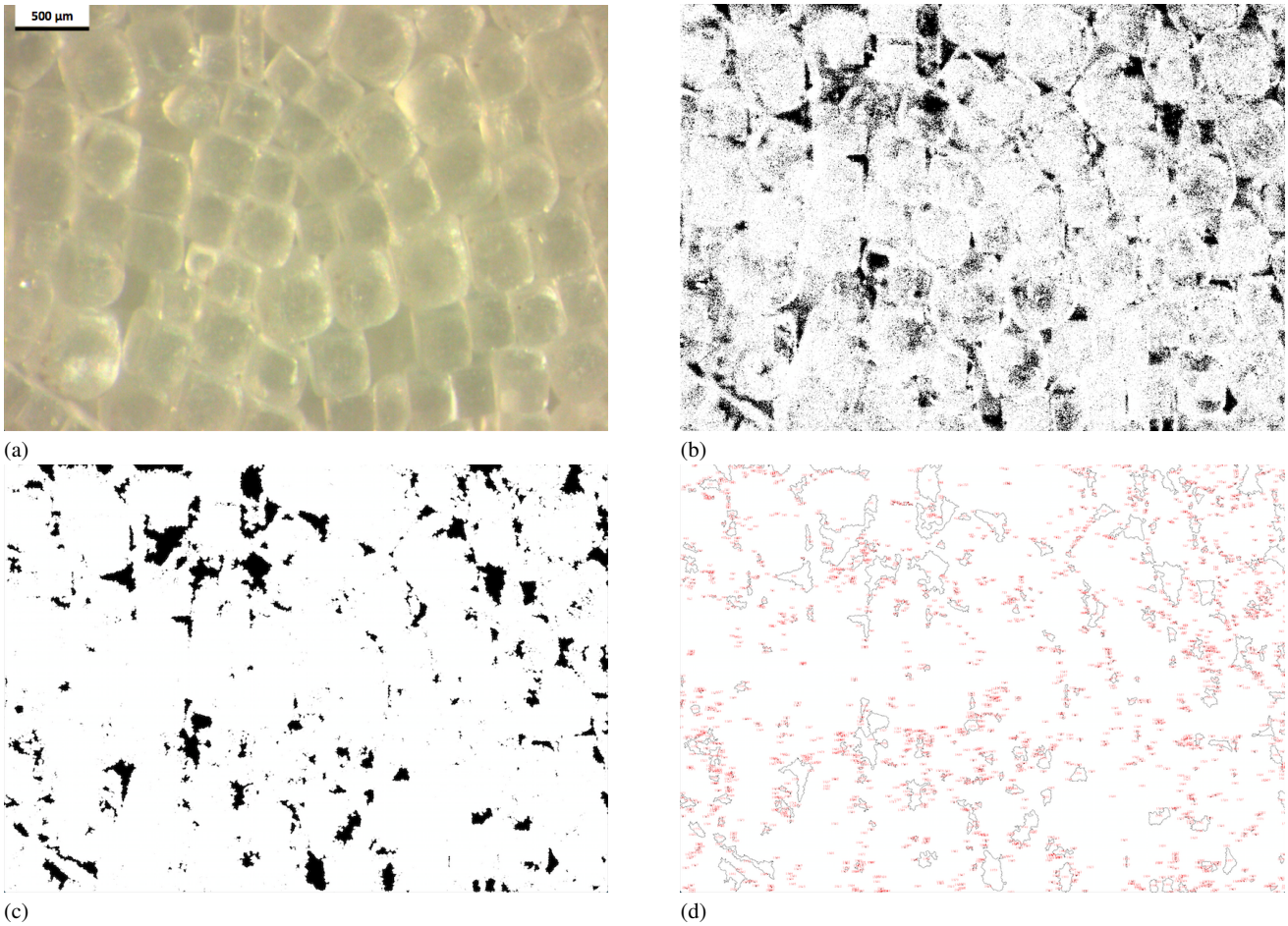

Fig. 6 Image processing: (a) Stereo-microscopic image; (b) Binary image; (c) Void distribution; (d) Void outline. Black lines represent the contours of the voids, which were assigned a number (written in red) by the program used for the image analysis.

opening and closure, and grain cementation corresponds to rebonding. Table 1 summarizes the construction of the proposed CDM model for crack debonding, opening, closure and rebonding. In the creep tests described above, inter-granular voids (analogs of micro-cracks) were observed in a plane containing the loading axis. The trace of the microscopic voids (analogs of cracks) in that plane was modeled with a fitting ellipse for simplicity (ellipses can be characterized by only two parameters: the major and minor semi-axis lengths). Ellipsoidal shapes capture the elongation and the decrease of volume of inter-granular voids, which is a sufficient model of crack debonding, opening, closure and rebonding. In the model, microscopic cracks are represented by ellipoids presenting a symmetry of revolution about the loading direction, as shown in Figure 8. REV damage is the result of material debonding. Therefore, the link between fabric changes and phenomenological variables is established as follows:

- During elastic loading or unloading, only crack aperture (λ_a) varies (Fig. 8a,c).
- When damage propagates, the crack length ($2\,R$) increases (Fig. 8b). The change of void area and crack length governs the change of aperture (λ_a) during the deformation that accompanies damage propagation.
- Healing of cracks perpendicular to the loading direction can only occur when deformation in the loading direction is compressive. When this condition is met, it is assumed that cracks perpendicular to the loading directions are closed, or almost closed, so that during healing (Fig. 8d), the crack length ($2\,R$) decreases but the crack aperture remains constant ($\Delta\lambda_a = 0$).

Equivalently, in the proposed CDM model (Table 1):

- The distributions of crack lengths $p(R_i)$ varies with the components of irreversible damage deformation ε_i^{id} and healing deformation ε_i^h.
- The distribution of void area projected in planes containing the loading axis $p(A_v)$ varies with total deformation $\boldsymbol{\varepsilon}$.
- The void area $A_v = 0.5\pi\lambda_a R$ varies:

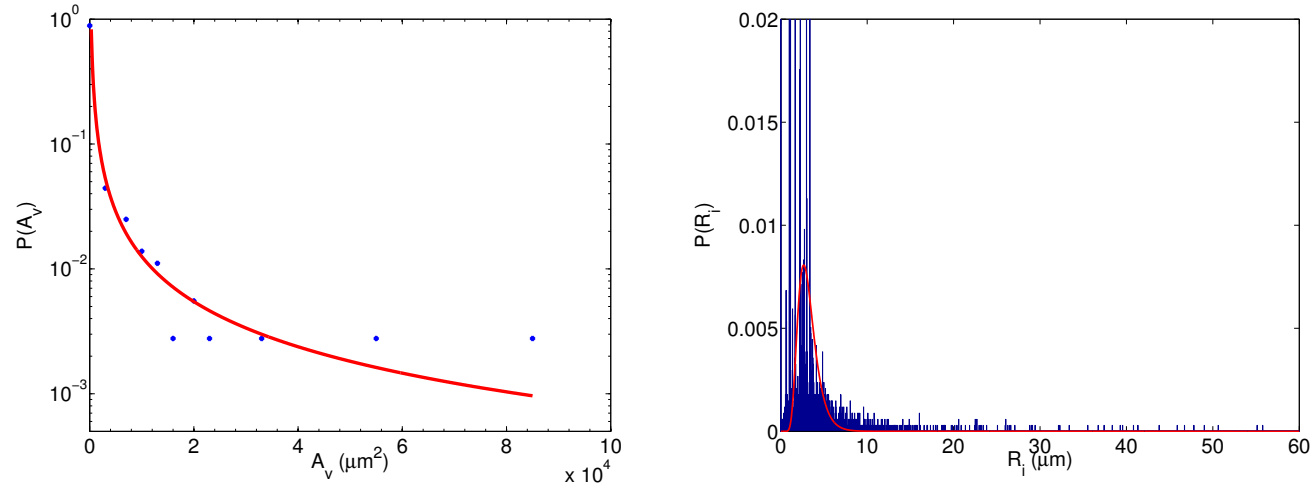

(a) (b)

Fig. 7 Probability density functions obtained for the void area (A) and for the crack length (defined as the major semi-axis of fitting ellipses projected in the three directions of space: R_i, i=x,y,z. (a) Power-law distribution of void area $p(A)$; (b) Log-normal distribution of crack length $p(R_i)$. *Note that the spikes are due to the presence of small black dots in the binary image obtained after processing. Image acquisitions will be improved in future work to address this issue, by utilizing non-transparent materials.*

– With the aperture λ_a only when net damage $\boldsymbol{A}$ does not evolve ($\Delta\boldsymbol{\varepsilon}^{id} = \Delta\boldsymbol{\varepsilon}^{h} = 0$):

$$\Delta A_v = \frac{\partial A_v}{\partial \lambda_a}\Delta\lambda_a, \qquad \frac{\partial A_v}{\partial R} = 0 \tag{23}$$

– With both the aperture and the crack length R when net damage $\boldsymbol{A}$ evolves:

$$\Delta A_v = \frac{\partial A_v}{\partial \lambda_a}\Delta\lambda_a, + \frac{\partial A_v}{\partial R}\Delta R \tag{24}$$

5.2 Relationship between fabric descriptors and phenomenological variables

The concept of crack density tensor (Kachanov 1992) is adapted to account for the difference of crack length in the three directions of space. Damage is defined as a second-order tensor. Assuming that the principal directions of stress and net damage are parallel, net damage eigenvalues are related to the means of the crack length components ($\overline{R}_j$) by:

$$\boldsymbol{A} = \sum_{j=1}^{3} A_j \boldsymbol{e_j} \otimes \boldsymbol{e_j} \tag{25}$$

$$A_1 = N_v \frac{(\overline{R}_2\overline{R}_3)^{\frac{3}{2}}}{V_{REV}},\ A_2 = N_v \frac{(\overline{R}_1\overline{R}_3)^{\frac{3}{2}}}{V_{REV}},\ A_3 = N_v \frac{(\overline{R}_1\overline{R}_2)^{\frac{3}{2}}}{V_{REV}} \tag{26}$$

In which N_v is the number of voids (i.e. micro-cracks) in the REV. As a result, it is possible to update the distributions of crack length components as follows:

$$\Delta\boldsymbol{\varepsilon} \rightarrow \Delta\boldsymbol{A} \underbrace{\rightarrow}_{\text{Eq. 26}} \overline{R}_1,\ \overline{R}_2,\ \overline{R}_3 \underbrace{\rightarrow}_{\overline{R}_j = \int R_j p_j(R_j) dR_j} p_j(R_j) \tag{27}$$

The two first moments of probability have to be used to update the mean and standard deviation of the probability density functions p_j. A sensitivity analysis (not presented in this paper) showed that the standard deviation shall not vary significantly in the conditions of pressure and temperature of the creep tests presented. Therefore in the following, the standard deviations are considered constant after initialization. Only the means m_i are updated, following a procedure similar to the one explained by Arson and Pereira (2013).

Under the assumption that grains are incompressible (i.e., that rearrangment and cementation only affect the voids between grains), the volumetric deformation of the REV is equal to the porosity change. The computation of porosity requires computing the three-dimensional volume of voids. However, microscopic observations only provide the void area. A linear interpolation is used:

$$\frac{n_{3D} - n_{3D,lower}}{n_{3D,upper} - n_{3D,lower}} = \frac{n_{2D} - n_{2D,lower}}{n_{2D,upper} - n_{2D,lower}} \tag{28}$$

In which n_{3D} (resp. n_{2D}) denotes the 3D (resp. 2D) porosity. "lower" and "upper" suscripts refer to the lower and upper bounds of the expected variations of porosity, respectively. Once the lower and upper bounds of 2D and 3D porosity are known, the probability density function of void area $p_A(A_v)$ can be updated with the 2D porosity:

$$\Delta\boldsymbol{\varepsilon} \rightarrow \Delta n_{3D} \underbrace{\rightarrow}_{\text{Eq. 28}} \Delta n_{2D} \underbrace{\rightarrow}_{\overline{n}_{2D} = \int \frac{A_v}{A_{REV}} p_A(A_v) dA} p_A(A_v) = a \times A_v^t \tag{29}$$

Table 1 Construction of the model of damage and healing (continuum REV) from microstructure observation (granular assembly)

	Crack debonding and opening	Crack closure	Crack rebonding
Granular Assembly	Grain rearrangement towards loose packing	Grain rearrangement towards tight packing	Cementation at grain faces
Continuum REV deformation	Purely elastic deformation $\boldsymbol{\varepsilon^{el}}$ and rate-independent damage deformation $\boldsymbol{\varepsilon^{ed}}$ (crack debonding) $+\boldsymbol{\varepsilon^{id}}$ (crack opening)	Rate-independent elastic deformation $\boldsymbol{\varepsilon^{E} = \varepsilon^{el} + \varepsilon^{ed}}$	Rate-dependent healing deformation $\boldsymbol{\varepsilon^{h}}$, counter-acting the irreversible damage deformation $\boldsymbol{\varepsilon^{id}}$
Continuum REV stiffness	Decrease of $\mathbb{C}(\boldsymbol{\Omega})$	Unilateral recovery under compression $H(-\boldsymbol{\varepsilon})\mathbb{C}_0$	Bilateral recovery

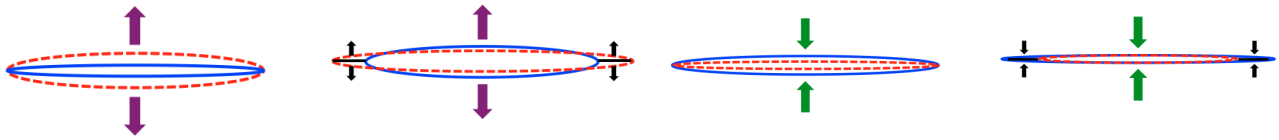

(a) Elastic tension (b) Non-elastic tension (c) Elastic unloading (d) Healing

Fig. 8 Representation of the geometric evolution of micro-cracks in the proposed model (solid line - original shape; dashed line - deformed shape): (a) Elastic tension: $\Delta\lambda_a \neq 0$, $\Delta R = 0$; (b) Non elastic tension: $\Delta\lambda_a \neq 0$, $\Delta R \neq 0$; (c) Elastic unloading (compression): $\Delta\lambda_a \neq 0$, $\Delta R = 0$; (d) Healing (after closure): $\Delta\lambda_a = 0$, $\Delta R \neq 0$

The two first moments of probability have to be used to update a and t probability parameters. Microscope observations indicate that t does not change significantly during the creep tests. In the following, t is fixed to the value fitted during the image analysis at the beginning of the creep tests, and only a is updated.

The lower bound of porosity is obtained at maximum packing. During creep regimes, salt grains tend to rearrange and form an ordered pattern, as illustrated in Figure 9. Table

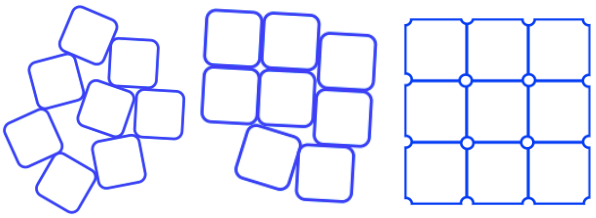

(a) Random packing (b) Rearrangement (c) Maximum packing

Fig. 9 Packing of table salt particles (2D view)

salt grains are not perfectly cubic, since the corners are rounded. Accordingly, the voids among particles at maximum packing are assumed to be spheres distributed in a periodic pattern, so that:

$$n_{2D,lower} = \frac{A_{v,lower}}{A_{REV}} = \frac{\pi r^2}{l^2} \tag{30}$$

$$n_{3D,lower} = \frac{V_{v,lower}}{V_{REV}} = \frac{\frac{4}{3}\pi r^3}{l^3} \tag{31}$$

In which A_v and V_v denote the area and the volume of the voids present in the REV, respectively. The edge length of salt grains l and the radius of the void spheres r are determined by microscopic observation.

In the present case, the upper bound of porosity is assumed to be reached in the initial state, when salt grains are assembled in a loose packing before the creep test. The void area at loose-packing ($A_{v,upper}$) and the total area of the zone captured (A_T) are obtained by microscopic observation:

$$n_{2D,upper} = \frac{A_{v,upper}}{A_T} \tag{32}$$

The 3D upper bound is approximated as:

$$n_{3D,upper} = \frac{V_{v,upper}}{V_T} \tag{33}$$

$$V_{v,upper} = V_T - V_s = A_{tube} \cdot L_{upper} - \frac{m_s}{\rho_s} \tag{34}$$

In which m_s is the mass of the dry table salt initially put in the tube, ρ_s is table salt mass density, and L_{upper} is the length of the sample enclosed between two rods in the tube.

5.3 Relationship between fabric descriptors and residual stress

By definition of the strain components (equation 1):

$$\boldsymbol{\sigma} = \mathbb{C}_0 : \boldsymbol{\varepsilon^{el}} - \tau \boldsymbol{K_0} = \mathbb{C}(\boldsymbol{\Omega}) : (\underbrace{\boldsymbol{\varepsilon^{el}} + \boldsymbol{\varepsilon^{ed}}}_{\boldsymbol{\varepsilon^{E}}}) - \tau \boldsymbol{K}(\boldsymbol{\Omega}) \quad (35)$$

In a strain-controlled test, $\Delta\boldsymbol{\varepsilon}$ is known. Once damage and stress are updated, equation 35 yields the elastic components of deformation ($\boldsymbol{\varepsilon^{el}}$ and $\boldsymbol{\varepsilon^{ed}}$). The irreversible deformation ($\boldsymbol{\varepsilon^{id}}$) is then obtained by difference, with equation 1. In isothermal conditions, the derivation of Equation 35 yields:

$$\begin{aligned} d\boldsymbol{\sigma} &= \mathbb{C}(\boldsymbol{\Omega}) : d\boldsymbol{\varepsilon^{E}} + \left(\frac{\partial \mathbb{C}(\boldsymbol{\Omega})}{\partial \boldsymbol{\Omega}} : \boldsymbol{\varepsilon^{E}} \right) : d\boldsymbol{\Omega} \\ &= \mathbb{C}(\boldsymbol{\Omega}) : d\boldsymbol{\varepsilon} - \mathbb{C}(\boldsymbol{\Omega}) : d\boldsymbol{\varepsilon^{id}} + \left[\frac{\partial \mathbb{C}(\boldsymbol{\Omega})}{\partial \boldsymbol{\Omega}} : (\boldsymbol{\varepsilon} - \boldsymbol{\varepsilon^{id}}) \right] : d\boldsymbol{\Omega} \\ &= \mathbb{C}(\boldsymbol{\Omega}) : d\boldsymbol{\varepsilon} + \frac{\partial \mathbb{C}(\boldsymbol{\Omega})}{\partial \boldsymbol{\Omega}} : \boldsymbol{\varepsilon} : d\boldsymbol{\Omega} - d(\mathbb{C}(\boldsymbol{\Omega}) : \boldsymbol{\varepsilon^{id}}) \\ &= \mathbb{C}(\boldsymbol{\Omega}) : d\boldsymbol{\varepsilon} + \frac{\partial \mathbb{C}(\boldsymbol{\Omega})}{\partial \boldsymbol{\Omega}} : \boldsymbol{\varepsilon} : d\boldsymbol{\Omega} + d\boldsymbol{\sigma_R} \end{aligned} \quad (36)$$

The derivations are similar when $\tau \neq 0$ and are not detailed here. Eq. 36 indicates that updating stress requires updating total deformation, damage and residual stress. Deformation and damage are related to fabric descriptors according to equations 27 and 29. The relationship between the residual stress and the distributions of void area (A_v) and crack length components (R_j) is established below.

The residual stress $\boldsymbol{\sigma_R}$ is the compressive stress that should be applied after unloading to neutralize the irreversible deformation due to remaining crack openings produced in tension (Eq. 2). Damage is the variable introduced to measure the energy dissipated by micro-crack "debonding". The concept of irreversible damage-induced deformation avoids resorting to a plastic potential to account for the dilatancy effects induced by micro-crack "opening". Irreversible damage deformation is originated by the geometric incompatibilities that prevent crack faces to be perfectly in contact after closure. Such incompatibilities may arise because of slip or gouge formation. In previous models of damage, the residual stress was assumed to be proportional to the damage tensor (e.g., Halm and Dragon 1998; Swoboda and Yang 1999; Arson and Gatmiri 2009; Xu and Arson 2014). Such an approach provides an averaged estimate of the energy dissipated by crack opening: all micro-cracks are assumed to have the same toughness and to respond identically to a normal stress applied in the far field, regardless of their shape and interactions. In the proposed model, the residual stress is related to fabric descriptors in order to account for micro-crack shape in the computation of the energy dissipated by opening.

Micro-cracks are assumed to be non-interacting, so that the solid matrix surrounding each crack is considered as an isotropic linear elastic material. The theory of fracture mechanics (Anderson 2005) is used to compute the micro-crack opening vector of an ellipsoidal micro-crack propagating in mode I (Figure 10). The micro-crack displacement in the direction perpendicular to the micro-crack axis writes (y-axis):

$$u_y(r,\theta) = \frac{K_I}{2\mu}\sqrt{\frac{r}{2\pi}} sin(\frac{\theta}{2})[\kappa + 1 - 2cos^2(\frac{\theta}{2})] \quad (37)$$

In which u_y is half of the crack aperture at location (r, θ), K_I is the stress intensity factor in mode I at the crack tip ($r = 0$), and μ is the shear modulus of the linear elastic bulk material. κ depends on the bulk Poisson's ratio ν: $\kappa = 3-4\nu$ in plane strain, $\kappa = \frac{3-\nu}{1+\nu}$ in plane stress.

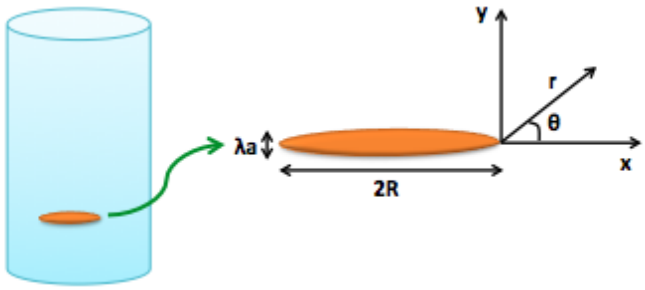

Fig. 10 Schematic representation of a micro-crack subjected to residual stress within the REV

The stress intensity factor depends on the microscopic residual stress $\boldsymbol{\sigma_r} = \sigma_r \boldsymbol{e_y} \otimes \boldsymbol{e_y}$ that applies to the micro-crack faces: $K_I = \sigma_r\sqrt{\pi R}$. Moreover, the half-aperture $0.5\,\lambda_a$ defined above is equal to the displacement u_y when $\theta = \pi$, and $r = R$, in which R is half of the crack length:

$$\frac{1}{2}\lambda_a = \frac{\kappa+1}{2\sqrt{2}\mu} R\,\sigma_r \quad (38)$$

Recalling that the void area is $A_v = 0.5\pi\lambda_a R$, the microscopic residual stress writes:

$$\sigma_r = \frac{\sqrt{2}\mu\lambda_a}{(\kappa+1)R} = \frac{2\sqrt{2}}{\pi}\frac{\mu}{\kappa+1}\frac{A_v}{R^2} \quad (39)$$

The non-interaction assumption allows writing the macroscopic residual stress as:

$$\sigma_R = N_v\sigma_r = N_v\frac{2\sqrt{2}}{\pi}\frac{\mu}{\kappa+1}\frac{A_v}{R^2} \quad (40)$$

Note that in equation 40, the index providing the direction of the projection was skipped for clarity. In the 3D space, residual stress is related to the crack length components (R_j, $j = x, y, z$):

$$\sigma_R^{(i)} = N_v\frac{2\sqrt{2}}{\pi}\frac{\mu}{\kappa+1}\frac{A_v}{R_j\,R_k} \quad \text{with} \quad i \neq j,\ j \neq k,\ k \neq i$$

(41)

The probability density functions of fabric descriptors are updated with deformation and damage (equations 27 and 29), and are then used as inputs to update the residual stress. This closes the formulation:

$$p_A(A_v),\ p_j(R_j) \underbrace{\rightarrow}_{\text{Eq. 41}} \sigma_R^{(i)} \underbrace{\rightarrow}_{\text{Eq. 36}} \boldsymbol{\sigma} \underbrace{\rightarrow}_{\text{Eq. 1, 35}} \boldsymbol{\varepsilon}^{el},\ \boldsymbol{\varepsilon}^{ed},\ \boldsymbol{\varepsilon}^{id} \quad (42)$$

The determination of the residual stress in equation 41 requires the computation of the mean of the probability $p(A_v/R_j\ R_k)$. Details are provided in the appendix.

5.4 Grain-scale model of DMT healing

The kinetics of healing are assumed to be governed by a general diffusion equation:

$$\frac{\partial u}{\partial t} = D_c \nabla^2 u \quad (43)$$

In which D_c is the diffusion coefficient, u represents the "intensity of net damage", defined as $u = U_0 - h$, and U_0 is the intensity of damage in the REV before healing occurs: $U_0 = tr(\boldsymbol{\Omega})_{t=0}$. The clock to measure time t is set to zero as soon as crack closure is achieved. As micro-cracks rebond, h increases and u decreases. Equation 43 governs DMT processes at the grain scale, and models the migration of sodium ions from salt grain bulk to salt grain boundaries. The maximum diffusion distance is half of the edge length of salt grains ($l/2$). The inter-granular space is an analog of microscopic cracks. Crack healing is complete when an ion reaches a crack face and electronic forces bonds this ion to the lattice of the opposite crack face. Therefore, in a local coordinate system with the origin set at the centroid of a grain, the following boundary conditions apply:

$$\begin{cases} u(x = -l/2, t) = 0 \\ u(x = l/2, t) = 0 \end{cases} \quad (44)$$

For a given time, it is assumed that all cracks in the REV are subjected to the same rate of healing. Therefore, the initial condition that holds to solve the diffusion equation is the same as the initial condition of healing at the REV scale:

$$h(x, t = 0) = 0, \qquad u(x, t = 0) = U_0 \quad (45)$$

The solution of the problem set in equations 43, 44 and 45 can be written as follows:

$$u(x,t) = \frac{4U_0}{\pi} \sum_{i=1,3,5,\ldots}^{\infty} \frac{e^{-\lambda_n^2 D_c t} sin(\lambda_n x)}{n} \quad (46)$$

In which:

$$\lambda_n = \frac{n\pi}{l} \quad (47)$$

The space average of the density of net damage u can be defined at the REV scale as:

$$\bar{u}(t) = < u(x,t) >= \frac{1}{l}\int_0^l u(x,t)dx$$
$$= \frac{8U_0}{\pi\, l} \sum_{n=1,3,5\ldots}^{\infty} \frac{e^{-\lambda_n^2 D_c t}}{n\lambda_n} \quad (48)$$

The normalized solution (for $U_0 = 1$) is plotted in Fig. 11. As time evolves, $\bar{u}(t)$ approaches zero. Ultimately, healing is completed when the normalized time $\tilde{t}$ reaches one, i.e. for a period of healing equal to the characteristic time $t = \frac{l^2}{D_c}$.

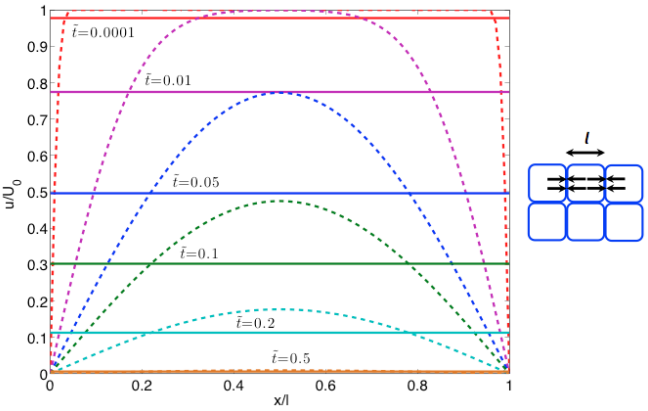

Fig. 11 Evolution law of normalized density of net damage ($\tilde{t} = \frac{D_c t}{l^2}$, $D_c = 10^{-12} m^2/s, l = 10^{-4} m, L_{REV} = 1m, U_0 = 1$)

Note that in general the diffusion coefficient D_c depends on both pressure and temperature. The simulations presented in the following assume that D_c only varies with temperature, since creep is observed at constant pressure. The constitutive model proposed by Weertman (1955) to predict diffusion within solids is adopted herein:

$$D_c = D_{c0}\, e^{-\frac{Q}{RT}} \quad (49)$$

In which D_{c0} is the maximum diffusion coefficient at infinite temperature, Q is the activation energy, T is temperature, R is the constant of perfect gases. More activation energy is required for a chloride ion to jump into a chloride vacancy than for a sodium ion to jump into a sodium ion vacancy (Mapother et al. 1950). Therefore, it can be reasonably assumed that diffusion of sodium chloride is due entirely to migration of the sodium ion. Mapother's study on the temperature dependence of self-diffusion coefficient (D_c) of sodium shows a linear relation in a log-scale plot:

$$D_c = -\frac{1.67 \times 10^{-12}}{T} + 2.99 \times 10^{-15} \quad (50)$$

In which T is expressed in Kelvin, D_c is in m^2/s. Note that the formula above was fitted to experimental results obtained during diffusion tests in sodium chloride within the range of temperature $573K \sim 973K$.

6 Stress Path Analysis: Crack Debonding, Opening, Closure and Rebonding during a Uniaxial Test

The one-dimensional stress path illustrated in Table 2 was programmed in MATLAB for a strain-controlled test. The porosity of the unit REV is entirely attributed to microscopic cracks, i.e. to inter-granular void space. Accordingly, the initial damage tensor is non-zero and the presence of micro-cracks implies that the initial residual stress is non-zero. Since total deformation is initially zero, the initial irreversible damage deformation is compensated by initial elastic deformation. In other words, elastic deformation energy is stored in the undamaged part of the solid skeleton. The initial crack distribution is characterized by the value of initial porosity (to initialize the probability density function of the void area) and the initial volumetric damage (to initialize the probability density function of the crack lengths). The solution of the diffusion equation averaged in space (Eq. 48) is approximated by truncating the infinite sum at $N = 100$.

6.1 Algorithm and Constitutive parameters

The macroscopic damage and healing model depends on seven mechanical parameters λ, μ, α, β, g, C_0, C_1 and one thermal parameter α_T. These parameters were calibrated for different types of rocks in a previous study by Zhu and Arson (2014). In the absence of relevant quantitative experimental datasets, macroscopic parameters could not be calibrated for salt rock. For illustrative purposes, a set of parameters fitted for sandstone is employed in the simulations presented in the following. Future investigations are needed to calibrate the macroscopic model by means of dedicated thermo-mechanical tests on salt rock. The microscopic parameters are determined as follows:

- The solution of the diffusion equation (Eq. 48) is normalized ($U_0 = 1$), and D_c is chosen according to equation 50.
- $n_{2D,lower}$, $n_{2D,upper}$, $n_{3D,lower}$, $n_{3D,upper}$, l are computed from equations 30, 31, 32 and 34, with data obtained from microscopic observation.
- The bounds of the fabric descriptors (A_{min}, A_{max}, R_{min}, R_{max}) are estimated as follows. The actual grain size of salt crystals is close to that of table salt grains, which is in the order of magnitude of 10^{-4}m. By definition, R cannot exceed the grain size, which was taken as an upper bound (R_{max}). The lower bound (R_{min}) was taken ten times smaller, which is an order of magnitude consistent with micro-cracks observed in clay stone [28]. Then, crack aperture was computed automatically by the program used for the simulations (Eq. 38): it was found to be about $10^3 - 10^4$ times smaller than the order of magnitude for crack length. The bounds for A_v, the void area, were estimated from the formula for the area of an ellipse.
- The exponent of the power-law distribution of the void area (Eq. 21) is determined from microscopic observation: $t = -1.2$.
- The number of voids N_v and the standard deviations of the distributions of crack length components (s_1, s_2, s_3) are computed in the initialization phase of the algorithm, and then kept constant.
- The means of void area and crack length components (a, m_1, m_2, m_3) are updated with the macroscopic phenomenological variables.

Table 2 summarizes the model parameters used in the simulations. Note that the soil mechanics sign convention is adopted, with tension counted negative.

6.2 Stress paths investigated

Numerical simulations were performed to study the influence of time and temperature on the healing process leading to mechanical recovery during application of the stress path shown in Figure 2. Mechanical loading and unloading before and after the healing process are carried out at room temperature (T_{room}), whereas the healing process takes place at temperature T_{heal}. In the simulations, healing takes place at constant axial strain, under zero lateral stress, and under constant temperature. Table 3 summarizes the simulation plan for this sensitivity analysis. Scenario 1 is taken as the reference case with a 10,000-second healing period at temperature $T_{heal} = 593K$ (room temperature is $293K$). The influence of time (respectively temperature) is studied with scenarios 2 and 3 (respectively scenarios 4 and 5). The value of the diffusion coefficient is updated with temperature according to Eq. 50.

Table 3 Simulation plan

Scenario	Duration (s)	T_{heal} (K)	D_c (m^2/s)
1 (ref)	10,000	593	1.74×10^{-16}
2	20,000	593	1.74×10^{-16}
3	30,000	593	1.74×10^{-16}
4	10,000	643	3.93×10^{-16}
5	10,000	693	5.80×10^{-16}

6.3 Results and interpretations

Parametric studies of the effect of time and temperature on healing are presented in Figures 12&13 and 14&15, respectively. The evolution of macroscopic variables is presented

Table 2 Model parameters used for the simulation of strain-controlled uniaxial tension loading/unloading/healing

λ (Pa)	μ (Pa)	α (Pa)	β (Pa)	g(Pa)	C_0 (Pa)	C_1 (Pa)	$\alpha_T(K^{-1})$	$U_0(-)$	l (m)
2.63×10^{10}	1.75×10^{10}	1.9×10^{9}	-2.04×10^{10}	1.1×10^{8}	1000	2.5×10^{5}	-1×10^{-5}	1	1×10^{-4}
$n_{2D,lower}(-)$	$n_{2D,upper}(-)$	$n_{3D,lower}(-)$	$n_{3D,upper}(-)$	$t(-)$	$R_{min}(m)$	$R_{max}(m)$	$A_{min}(m^2)$	$A_{max}(m^2)$	$e_0(-)$
0.03	0.165	0.004	0.321	-1.2	1×10^{-5}	1×10^{-4}	1×10^{-14}	1×10^{-12}	0.008

first (Figures 12&14), followed by the evolution of microscopic variables (Figures 13&15). The stress/strain plots obtained numerically (Figures 12.a and 14.a) follow the expected trends (illustrated in Figure 3): the slope first decreases due to damage propagation (AB); unilateral effects are noted during the compression phase (DE); internal compressive stress develops due to the restrained thermal expansion of the sample during the creep phase at high temperature (EF), and partial mechanical recovery is achieved after the healing phase (FG_1). Additional damage is produced after recovery (G_1H) when the new damage threshold is reached (larger than the initial threshold but smaller than the threshold obtained after the tension phase).

The evolution of damage ($\boldsymbol{\Omega}$) is the same in all simulations (Figures 12.b and 14.b): micro-cracks do not propagate during the elastic loading phase (OA); damage ($\boldsymbol{\Omega}$) increases during the non-elastic tension phase (AB) remains constant during unloading, healing and elastic reloading (BCDEFG) and increases again during reloading after the new damage threshold is reached (GH). Net damage variable ($\boldsymbol{A}$) increases when damage increases, and decreases when healing increases. The model captures time-independent damage induced by thermo-mechanical tension or compression (Eq. 9, 10), and time-dependent healing under compression. For the stress paths simulated, cracks propagate in planes normal to the loading axis (direction 1), therefore, by definition of the damage variable (Eq. 26), only the first eigenvalue of damage is non-zero ($\Omega_1 \neq 0$, $\Omega_2 = \Omega_3 = 0$). During the healing phase at high temperature, internal compressional stress develops due to the restrained thermal expansion of the sample in the axial direction (EF). However this compression remains below the compression strength, and therefore, damage does not propagate during the creep phase. Net damage follows the same trends (Figures 12.d and 14.d), except after the unloading phase: during the creep process at constant axial deformation (EF), h increases due to crack rebonding, which results in a step-wise decrease of A_1. After that, the plots of A_1 and Ω_1 coincide again, except for the shift by the amount of h. Stiffness recovery is more important for longer healing periods and higher healing temperatures, as can be seen from the time evolution of $u = 1 - h$, the normalized intensity of net damage (Figures 12.c and 14.c). Note that after a period of healing of 30,000 seconds (about 8.5 hours) at 593K, the healing variable is equal to 5.4%, which corresponds to the decrease noted for net damage: A_1 drops from 16.8% to 11.4%. After 10,000 seconds (about 3 hours), healing is 3.8% at 593K: 1.5 times as much healing is achieved after three times as much healing time. A similar level of healing can be achieved after 8.5 hours at 593K and after 3 hours at 693K.

Figures 13 and 15 show the evolution of the fabric descriptors for the stress paths simulated. Due to the axis-symmetry of the problem and by construction of the model, microscopic cracks propagate only in planes orthogonal to direction 1 (loading axis), therefore crack lengths are non-zero only in directions 2 and 3 ($\overline{R}_2 = \overline{R}_3 \neq 0$, $\overline{R}_1 = 0$). According to the definition of net damage (Eq. 26), the evolution of crack lengths follows the evolution of net damage. The difference of convexity in plots 12.d,14.d on the one hand, and 13.b,15.b on the other hand is due to the cubic relationship between the eigenvalues of net damage and crack length. The mean of void areas is proportional to the porosity of the sample (Eq. 28, 29), which is assumed to vary like the volumetric deformation. In the tests simulated, axial deformation is about three times larger than lateral deformation, therefore volumetric deformation mostly varies with axial deformation. As a result, the mean of the void area evolves quasi-linearly with axial deformation during the mechanical loading and unloading phases (Figures 13.a and 15.a). During the healing phase, crack lengths shorten while crack apertures remain constant (according to the modeling assumptions summarized in Figure 8), therefore, overall the mean void area decreases. Note that the drop observed for the void area during the healing phase is equal to the drop of crack length times 10^{-9}m, which is the order of magnitude of the crack aperture.

According to the modeling assumptions (Figure 8), crack aperture varies linearly with axial deformation during elastic loading and unloading, and remains constant during the healing phase (Figures 13.c and 15.c). When damage propagates, crack lengths increase (due to crack debonding) and the void area increases (due to crack opening). The variations of aperture λ_a are computed in order to ensure the compatibility between the changes of crack length and the changes of crack area. For the present set of simulations,

crack aperture decreases when damage propagates, which means that micro-cracks become longer but thinner during propagation. Note that the maximum change of crack aperture during the tests is 10,000 times smaller than the maximum change of crack length, and is therefore negligible. Initially, the residual stress is non-zero, due to the presence of initial damage in the sample (Figures 13.d and 15.d). The residual stress varies linearly with the mean void area during the elastic loading and unloading phases, which is in agreement with the assumptions made in the model (Eq. 54-56). During the healing phase, crack aperture does not vary: the residual stress decreases with crack lengths (Figure 8). During crack propagation, the residual stress varies with both crack lengths and void area. In the present set of simulations, the evolution of the residual stress during crack propagation is dominated by the evolution of the void area. The link between microstructure changes and macroscopic variables is complex and will require further analyses with different stress paths and different fabric descriptors.

7 Conclusion

Geotechnical reservoirs and repositories in rocks such as nuclear waste disposals, geothermal systems, and high-pressure gas reservoirs are subjected to high stress and temperature gradients. In salt rock, creep microscopic processes are mainly glide, cross-slip, diffusion and dynamic recrystallization. Diffusive Mass Transfer (DMT) can result in crack rebonding, and therefore, to mechanical stiffness recovery. Crack rebonding driven by DMT occur wihin a few days at room temperature and low pressure. DMT is enhanced at higher temperatures, which could be beneficial for the sustainabilty of geological storage facilities in salt mines. On the one hand, visco-plastic laws relating creep microscopic processes to microstructure changes are empirical. On the other hand, theoretical models of damage and healing disconnect thermodynamic variables from their physical meaning. Moreover, crack closure and crack rebonding have not been modeled within the same Continuum Damage Mechanics (CDM) framework so far.

The proposed model enriches the CDM framework with fabric descriptors. In order to infer the form of fabric tensors from microstructure observation, creep tests were carried out on granular salt under constant stress and humidity conditions. The rearrangement of salt particles and the rebonding of grain boundaries during creep were described by the probability density functions of two geometric descriptors: the void area and the crack lengths. Macroscopic variables used in the damage and healing model are functions of moments of probability of void area and crack lengths. The free energy of the Representative Elementary Volume (REV) is written in the form of a polynomial comprising a purely thermo-elastic potential and a damaged energy component. Crack closure is considered by adopting the concept of unilateral effect on rock stiffness. Crack rebonding is assumed to result from Diffusive Mass Transfer (DMT) processes. Net damage evolution obeys a diffusion equation in which the characteristic time scales with the typical size of a grain of salt. The diffusion coefficient depends on temperature, which allows capturing the acceleration of healing at higher temperature.

The constitutive model was programmed at the integration point (in MATLAB) to simulate thermo-mechanical loading and unloading cycles in axis-symmetric conditions. A stress path comprising a tensile loading, a compressive unloading, a creep-healing stage and a reloading was simulated for different healing periods and temperatures. Macroscopic and microscopic model predictions are in agreement with the assumptions made in the constitutive framework, and highlight the increased efficiency of healing with time and temperature. For typical rock properties and loading conditions, a similar level of healing was achieved after a period of hold of 8.5 hours at 593K and after a period of hold of 3 hours at 693K. More experimental data is needed to properly calibrate the model and improve the predictions of stiffness, deformation and fabric for different stress paths. The concept of fabric enrichment is expected to bring new developments in Continuum Mechanics of damage and healing. The specific constitutive model presented in this paper is expected to improve the fundamental understanding of damage and healing in rocks at both macroscopic and microscopic levels, and to allow predicting the long-term behavior of geological storage facilities.

Acknowledgements

The authors are grateful to Professor J.C. Santamarina for his inspiring suggestions on the set up of the creep experiments presented in this manuscript.

Appendix A1: Relationship between the residual stress and the probability density functions of void area and crack length components

According to Eq. 41,

$$\sigma_R^{(i)} = N_v \frac{2\sqrt{2}}{\pi} \frac{\mu}{\kappa+1} M_i \tag{51}$$

In which:

$$M_i = \frac{A_v}{R_j\, R_k} \tag{52}$$

M_i is a random variable, defined as the product of three independent random variables: A_v, $z_j = 1/R_j$ and $z_k =$

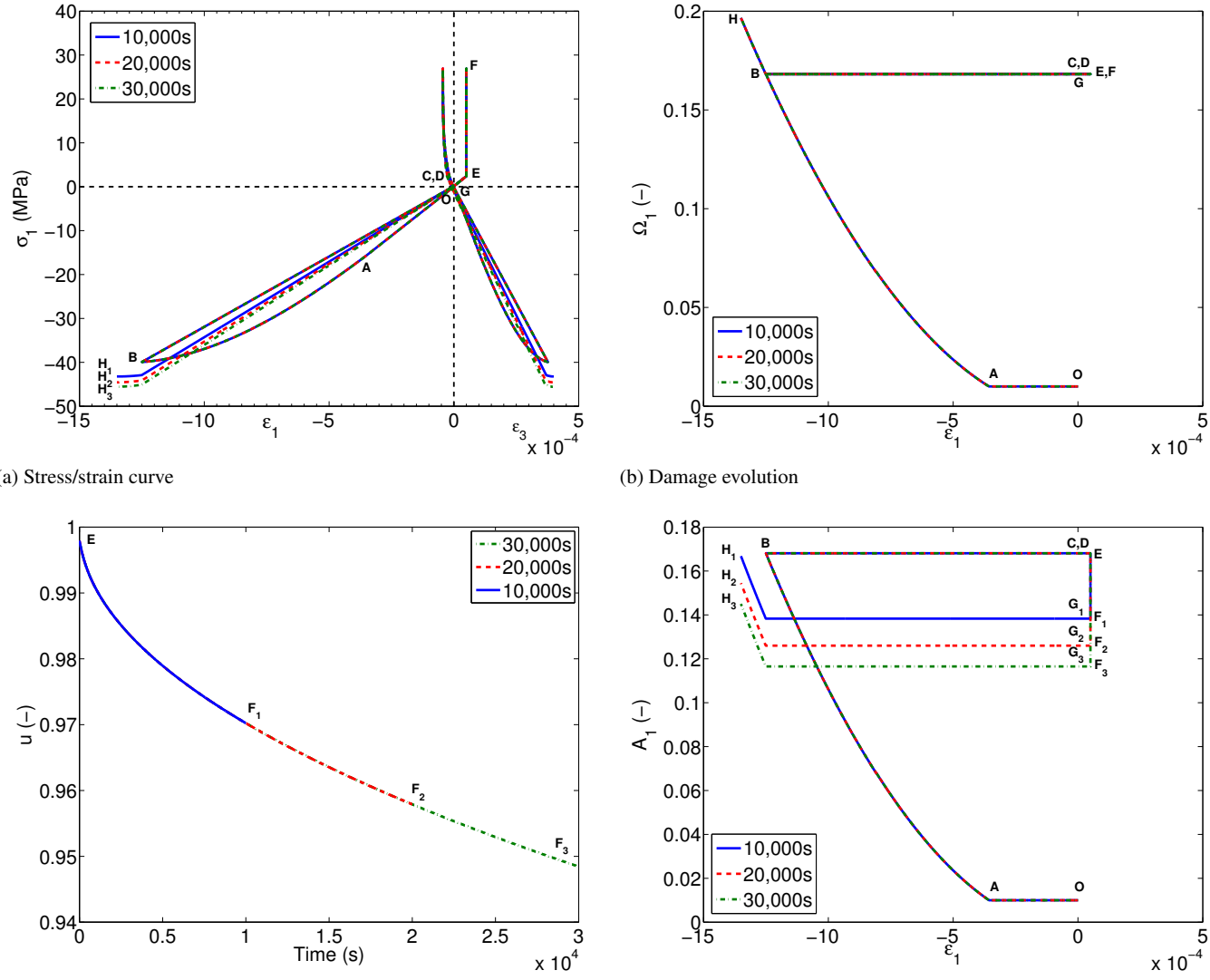

(a) Stress/strain curve

(b) Damage evolution

(c) Evolution of the normalized intensity of net damage

(d) Evolution of net damage

Fig. 12 Influence of healing time on mechanical recovery: macroscopic variables (direction 1 is the direction of tensile loading)

$1/R_k$. Therefore, the probability of M_i writes:

$$p(M_i) = p_A(A_v) \times p_{zj}(z_j) \times p_{zk}(z_k) \tag{53}$$

The components of the residual stress are updated with the means of M_1, M_2 and M_3, noted $\overline{M}_1$, $\overline{M}_2$ and $\overline{M}_3$ respectively:

$$\sigma_R^{(i)} = N_v \frac{2\sqrt{2}}{\pi} \frac{\mu}{\kappa+1} \overline{M}_i \tag{54}$$

$$\overline{M}_i = \int_{A_{min}}^{A_{max}} \int_{1/(R_{max})^2}^{1/(R_{min})^2} A_v \times z_j \times z_k \times p_A(A_v) \times p_{z_j}(z_j) \times p_{z_k}(z_k)\, dz_k dz_j dA \tag{55}$$

In the expression 56 above, we have:

$$p_A(A_v) = a A_v^t \tag{56}$$

The probability $p_{zj}(z_j)$ is obtained by differentiating the cumulative density function $F_j^*(z_j) = p_{zj}(z \leq z_j)$:

$$p_{zj}(z_j) = \frac{dF_j^*(z_j)}{dz_j} \tag{57}$$

With:

$$F_j^*(z_j) = p_{zj}(R^{-1} \leq z_j) = p_j(R \geq z_j^{-1}) \tag{58}$$

$$F_j^*(z_j) = 1 - p_j(R \leq z_j^{-1}) = 1 - F_j(z_j^{-1}) \tag{59}$$

Therefore:

$$p_{zj}(z_j) = -\frac{dF_j(z_j^{-1})}{dz_j} = -\underbrace{\frac{dF_j(z_j^{-1})}{d(z_j^{-1})}}_{p_j(z_j^{-1})} \underbrace{\frac{dz_j^{-1}}{dz_j}}_{-z_j^{-2}} \tag{60}$$

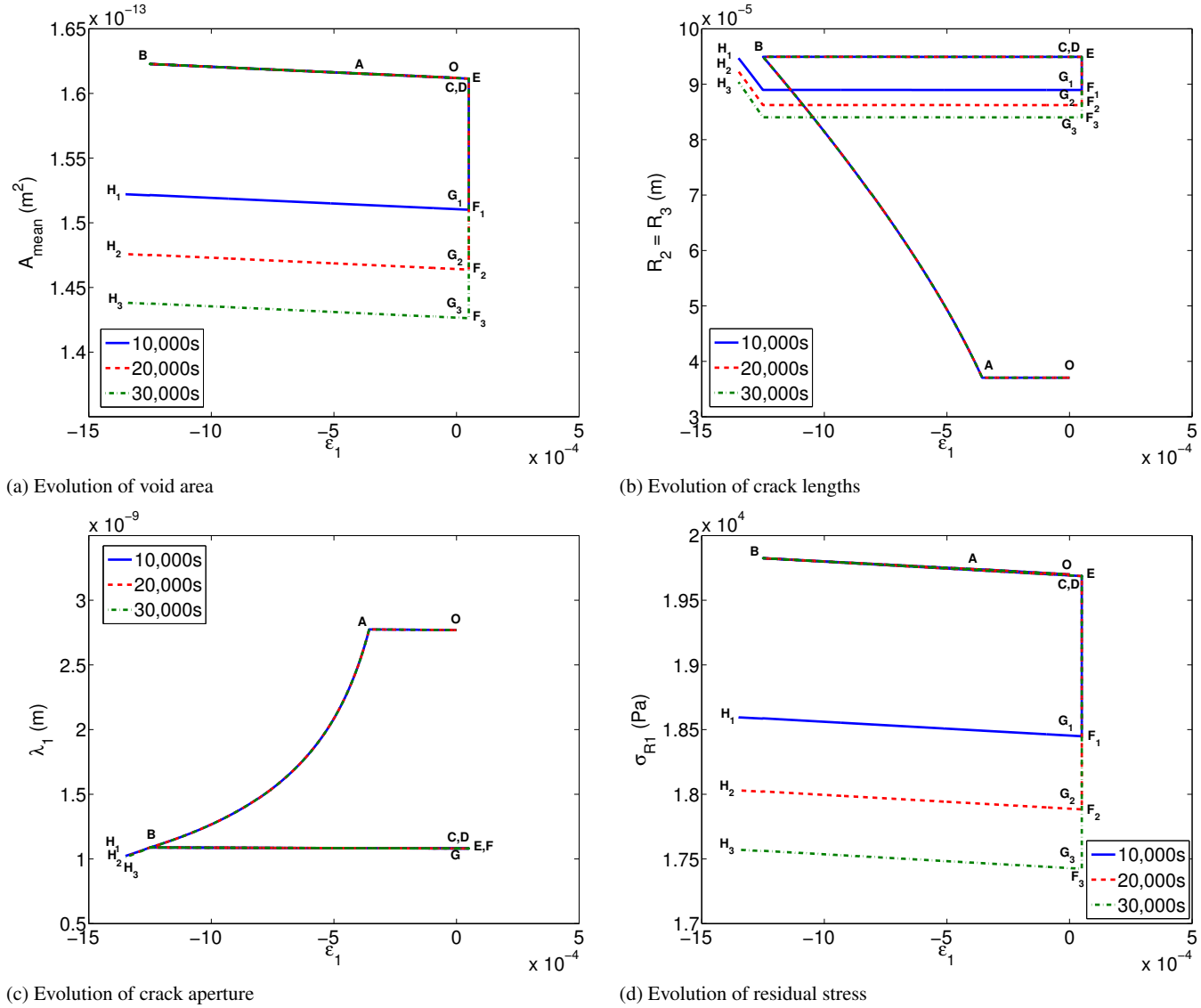

(a) Evolution of void area

(b) Evolution of crack lengths

(c) Evolution of crack aperture

(d) Evolution of residual stress

Fig. 13 Influence of healing time on mechanical recovery: residual stress and microscopic variables (direction 1 is the direction of tensile loading)

As a result:

$$p_{zj}(z_j) = p_j(z_j^{-1}) \times (z_j)^{-2} \tag{61}$$

Using the expression of the probability density function of the crack length components:

$$p_{zj}(z_j) = \frac{z_j^{-1}}{\sqrt{2\pi}\, s_j} exp\left[-\frac{\left(ln\left(z_j^{-1}\right) - m_j\right)^2}{2s_j^2} \right] \tag{62}$$

By this means, the residual stress can be derived from the fabric descriptors, i.e. from the void area and the crack length components.

Appendix A2: Table of Notations

References

Abràmoff MD, Magalhães PJ, Ram SJ (2004) Image processing with imagej. Biophotonics international 11(7):36–42

Anderson T (2005) Fracture Mechanics: Fundamentals and Applications, Third Edition. Taylor & Francis, URL http://books.google.com/books?id=MxrtsC-ZooQC

Arson C, Gatmiri B (2009) A mixed damage model for unsaturated porous media. Comptes Rendus Mécanique 337(2):68–74

Arson C, Gatmiri B (2012) Thermo-hydro-mechanical modeling of damage in unsaturated porous media: Theoret-

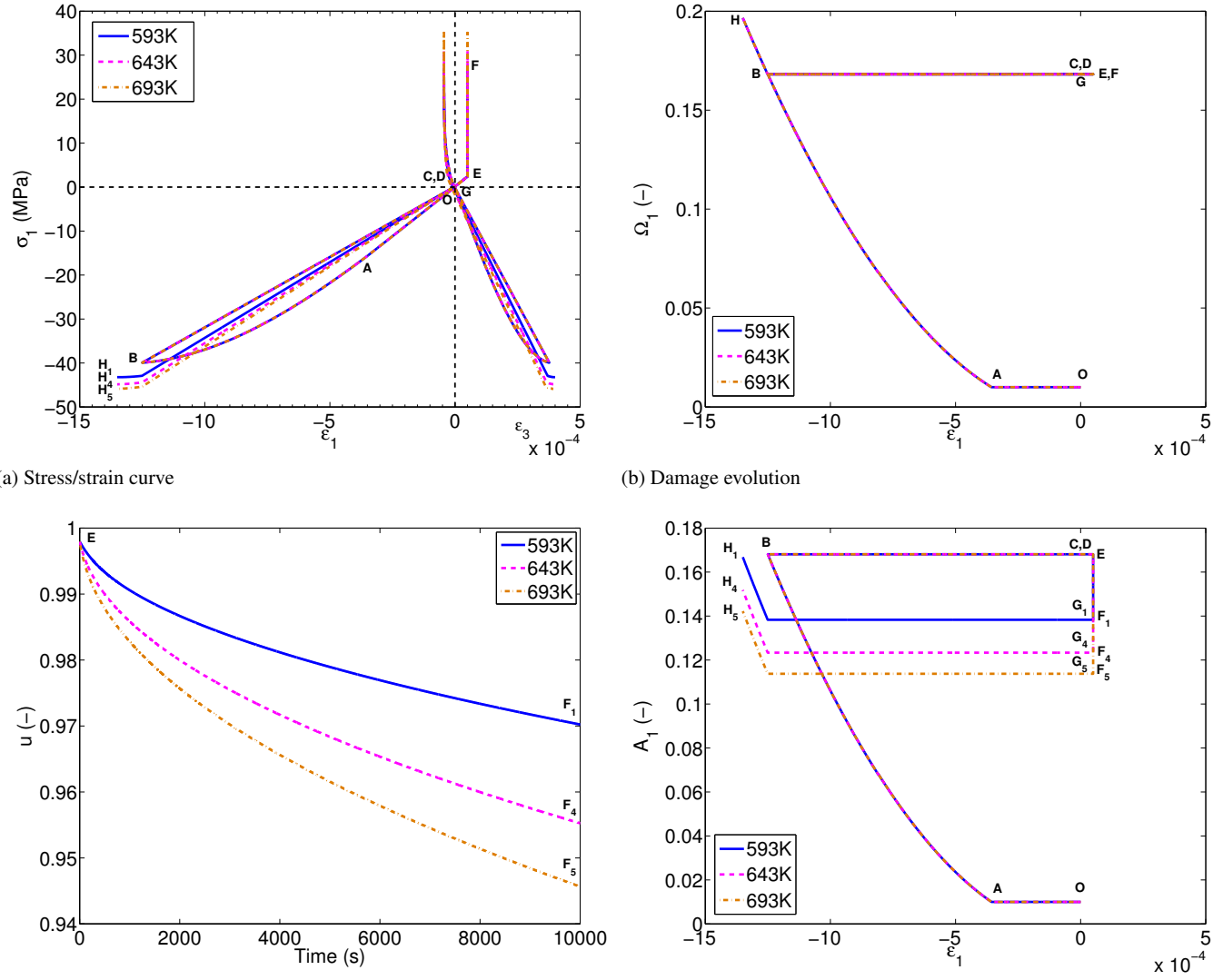

(a) Stress/strain curve

(b) Damage evolution

(c) Evolution of the normalized intensity of net damage

(d) Evolution of net damage

Fig. 14 Influence of healing temperature on mechanical recovery: macroscopic variables (direction 1 is the direction of tensile loading)

ical framework and numerical study of the edz. International Journal for Numerical and Analytical Methods in Geomechanics 36:272–306

Arson C, Pereira JM (2013) Influence of damage on pore size distribution and permeability of rocks. International Journal for Numerical and Analytical Methods in Geomechanics 37:810–831

Arson C, Xu H, Chester F (2012) On the definition of damage in time-dependent healing models for salt rock. Géotechnique Lett 2(April-June):67–71

Bérest P, Bergues J, Brouard B, Durup J, Guerber B (2001) A salt cavern abandonment test. International Journal of Rock Mechanics and Mining Sciences 38(3):357–368

Berest P, Brouard B, Karimi-Jafari M, Van Sambeek L (2007) Transient behavior of salt caverns - interpretation of mechanical integrity tests. International Journal of Rock Mechanics and Mining Sciences 44(5):767–786

Brodsky N, Munson D (1994) Proc. first n. amer. rock mech. symp. In: Nelson P, Laubach S (eds) Proc. First N. Amer. Rock Mech. Symp., pp 731–738

Chaboche JL (1992) Damage induced anisotropy: on the difficulties associated with the active/passive unilateral condition. Int J Damage Mech 1(2):148–171

Chan K, Bodner S, Munson D (1998) Recovery and healing of damage in wipp salt. Int J Damage Mech 7(2):143–166

Chan K, Bodner S, Munson D (2001) Permeability of WIPP salt during damage evolution and healing. Int J Dam-

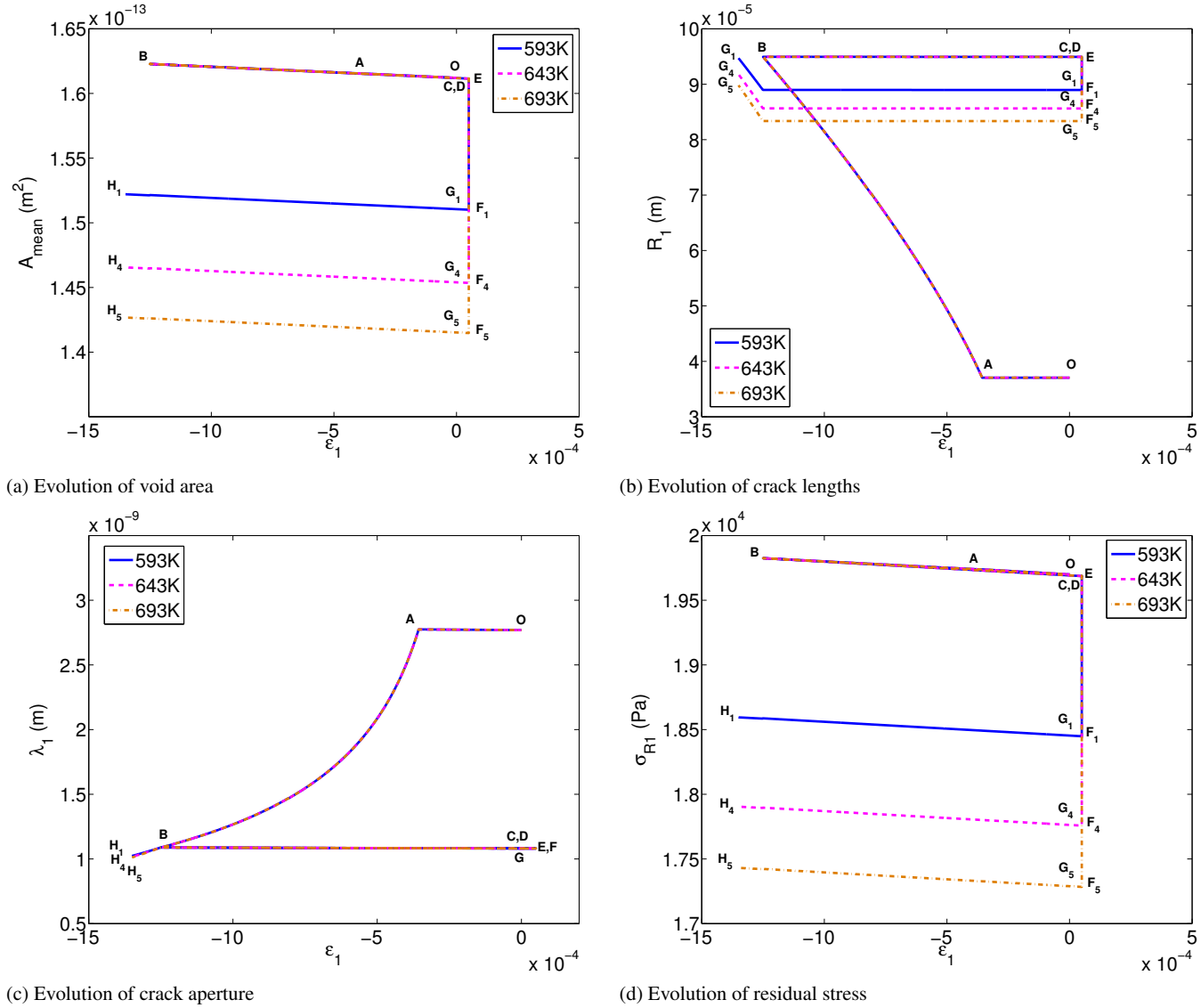

(a) Evolution of void area

(b) Evolution of crack lengths

(c) Evolution of crack aperture

(d) Evolution of residual stress

Fig. 15 Influence of healing temperature on mechanical recovery: residual stress and microscopic variables (direction 1 is the direction of tensile loading)

age Mech 10(4):347–375

Collins I, Houlsby G (1997) Application of thermomechanical principles to the modelling of geotechnical materials. Proceedings of the Royal Society of London Series A: Mathematical, Physical and Engineering Sciences 453(1964):1975–2001

Cosenza P, Ghoreychi M, Bazargan-Sabet B, De Marsily G (1999) In situ rock salt permeability measurement for long term safety assessment of storage. International Journal of Rock Mechanics and Mining Sciences 36(4):509–526

Dragon A, Halm D, Désoyer T (2000) Anisotropic damage in quasi-brittle solids: modelling, computational issues and applications. Comput Methods Appl Mech Eng 183(3):331–352

Fam M, Santamarina J, Dusseault M (1998) Wave-based monitoring processes in granular salt. Journal of Environmental and Engineering Geophysics 3(1):15–26

Fuenkajorn K, Phueakphum D (2011) Laboratory assessment of healing of fractures in rock salt. Bulletin of Engineering Geology and the Environment 70(4):665–672

Halm D, Dragon A (1998) An anisotropic model of damage and frictional sliding for brittle materials. Eur J Mech Solids 17(3):439–460

Hou Z (2003) Mechanical and hydraulic behavior of rock salt in the excavation disturbed zone around underground facilities. Int J Rock Mech Min Sci 40(5):725–

$\boldsymbol{\varepsilon^{el}}$	elastic deformation
$\boldsymbol{\varepsilon^{d}}$	damage-induced deformation
$\boldsymbol{\varepsilon^{ed}}$	damage-induced elastic deformation
$\boldsymbol{\varepsilon^{id}}$	damage-induced irreversible deformation
ε_v^E	volumetric elastic deformation
$\boldsymbol{\sigma_R}$	residual stress
$\boldsymbol{\Omega}$	damage tensor
$\mathbb{C}$	elasticity tensor
$\mathbb{C}_0$	elasticity tensor of undamaged material
$\mathbb{C}^*$	partially recovered stiffness due to unilateral effect
$\overline{\mathbb{C}}$	partially recovered stiffness due to healing
ψ_s^{ET}	purely thermo-elastic deformation energy
$\psi_s^{\Omega T}$	potential energy of crack faces
τ	temperature variation
C	heat capacity
C_0	heat capacity of undamaged material
C^*	partially recovered heat capacity due to unilateral effect
$\overline{C}$	partially recovered capacity due to healing
k	bulk modulus
α_T	thermal dilation coefficient
n	porosity
$\boldsymbol{\delta}$	second-order identity tensor
$\boldsymbol{K}$	diagonal tensor
λ, μ	Lame coefficients
α, β	damage parameters
$\boldsymbol{Y}$	damage driving force
$\boldsymbol{Y_d}$	active damage driving force
f_d	damage potential
$\boldsymbol{P_i}$	fourth order project tensor
$\boldsymbol{H}$	healing tensor
$\boldsymbol{A}$	mixed damage variable
A_v	void area
A_T	total area of the zone captured
R	crack length
λ_a	crack aperture
N_v	number of voids
$\overline{R}$	mean of the crack length components
n_{3D}	3D porosity
n_{2D}	2D porosity
l	edge length of salt grains
r	radius of void sphere
m_s	mass of dry table salt
ρ_s	table salt mass density
A_{tube}	inner cross-sectional area of the tube
L_{upper}	length of the sample enclosed between two rods
u_y	half of the crack aperture
K_I	stress intensity factor in mode I
κ	a function of bulk Poisson's ratio ν
u	intensity of net damage
$\overline{u}(t)$	space average of the density of net damage
D_c	diffusion coefficient
U_0	intensity of damage in the REV before healing occurs
t	healing time
Q	activation energy
T	healing temperature

738

Hunsche U, Hampel A (1999) Rock salt — the mechanical properties of the host rock material rock salt - the mechanical properties of the host rock material for a radioactive waste repository. Eng Geol 52(3-4):271–291

Kachanov M (1992) Effective elastic properties of cracked solids: critical review of some basic concepts. Appl Mech Rev 45(8):304–335

Kessler M, White S (2001) Self-activated healing of delamination damage in woven composites. Composites Part A: applied science and manufacturing 32(5):683–699

Kim HM, Rutqvist J, Ryu DW, Choi BH, Sunwoo C, Song WK (2012) Exploring the concept of compressed air energy storage (caes) in lined rock caverns at shallow depth: a modeling study of air tightness and energy balance. Applied Energy 92:653–667

Kwon S, Wilson J (1999) Deformation mechanism of the underground excavations at the WIPP site. Rock Mechanics and Rock Engineering 32(2):101–122

Li G, Uppu N (2010) Shape memory polymer based self-healing syntactic foam: 3-d confined thermomechanical characterization. Composites Science and Technology 70(9):1419–1427

Lux K, Eberth S (2007) Fundamental and first application of a new healing model for rock salt. Basic and Applied Salt Mechanics pp 129–138

Lux K, Düsterloh U, Hou Z (2000) Increasing the profitability of storage caverns by means of a new dimensioning concept (i). Erdöl Erdgas Kohle 118:294–300

Maleki K (2004) Modélibation numérique du couplage entre l'endommagement et la perméabilité des roches. application à l'érude des ouvrages de stockage souterrain. PhD thesis, Ecole Nationale des Ponts et Chaussées

Mapother D, Crooks HN, Maurer R (1950) Self-diffusion of sodium in sodium chloride and sodium bromide. The Journal of Chemical Physics 18:1231

Miao S, Wang M, Schreyer H (1995) Constitutive Models for healing of material with application to compaction of crushed rock-salt. JOURNAL OF ENGINEERING MECHANICS-ASCE 121(10):1122–1129

O'Connell RJ, Budiansky B (1974) Seismic velocities in dry and saturated cracked solids. Journal of Geophysical Research 79(35):5412–5426

Schulze O (2007) Investigations on damage and healing of rock salt. Mechanical Behavior of Salt-Understanding of THMC Processes in Salt pp 33–43

Senseny P, Hansen F, Russell J, Carter N, Handin J (1992) Mechanical behaviour of rock salt: phenomenology and micromechanisms. International journal of rock mechanics and mining sciences & geomechanics abstracts 29(4):363–378

Shao JF, Rudnicki J (2000) A microcrack-based continuous damage model for brittle geomaterials. Mechanics of Materials 32(10):607–619

Succar S, Williams RH (2008) Compressed air energy storage: Theory, resources, and applications for wind power. Princeton Environmental Institute Report 8

Swoboda G, Yang Q (1999) An energy-based damage model of geomaterials—i. formulation and numerical

902 results. International journal of solids and structures
903 36(12):1719–1734
904 Voyiadjis GZ, Shojaei A, Li G (2011) A thermody-
905 namic consistent damage and healing model for self
906 healing materials. International Journal of Plasticity
907 27(7):1025–1044
908 Weertman J (1955) Theory of steady-state creep based
909 on dislocation climb. Journal of Applied Physics
910 26(10):1213–1217
911 Wexler A, Hasegawa S (1954) Relative humidity-
912 temperature relationships of some saturated salt
913 solutions in the temperature range o ° to 50 ° c. Journal
914 of Research of the National Bureau of Standards
915 53(1):19–26
916 Xu H, Arson C (2014) Anisotropic damage models for ge-
917 omaterials: Theoretical and numerical challenges. In-
918 ternational Journal of Computational Methods 11:DOI:
919 10.1142/S0219876213420,073
920 Yow J, Hunt J (2002) Coupled processes in rock mass per-
921 formance with emphasis on nuclear waste isolation. In-
922 ternational journal of rock mechanics and mining sci-
923 ences 39(2):143–150
924 Zhou H, Hu D, Zhang F, Shao J (2011) A thermo-
925 plastic/viscoplastic damage model for geomaterials.
926 Acta Mechanica Solida Sinica 24(3):195 – 208
927 Zhu C, Arson C (2013) Modeling the influence of thermo-
928 mechanical crack opening and closure on rock stiff-
929 ness. In: Poromechanics V, pp 2526–2535
930 Zhu C, Arson C (2014) A thermo-mechanical damage model
931 for rock stiffness during anisotropic crack opening and
932 closure. Acta Geotechnica pp DOI: 10.1007/s11,440–
933 013–0281–0